LETTER

X-Shaped Bulge Preferred Over Dark Matter in the Galactic Center Gamma-Ray Excess

Oscar Macias[1], Chris Gordon[2], Roland M. Crocker[3], Brendan Coleman[2], Dylan Paterson[2], Shunsaku Horiuchi[1] & Martin Pohl[4,5]

[1]Center for Neutrino Physics, Department of Physics, Virginia Tech, Blacksburg, VA 24061, USA [2]Department of Physics and Astronomy, Rutherford Building,University of Canterbury, Private Bag 4800, Christchurch 8140, New Zealand [3]Research School of Astronomy and Astrophysics, Australian National University, Canberra, Australia [4]Institute of Physics and Astronomy, University of Potsdam, 14476 Potsdam-Golm, Germany [5]DESY, Platanenallee 6, 15738 Zeuthen, Germany

An anomalous excess emission has been found in Fermi Large Area Telescope (LAT) data[1] covering the centre of the Galaxy[2–7]. Several theories have been proposed for this 'Galactic Centre Excess' (GCE). They include self-annihilation of dark matter particles[2–6], an unresolved population of millisecond pulsars[3,4], an unresolved population of young pulsars[8], or a series of burst events[9]. We report on new analyses that exploit hydrodynamical modelling to register the position of interstellar gas associated with diffuse Galactic gamma-ray emission. We find evidence that the GCE gamma rays are statistically better described by the X-shaped stellar over-density in the Galactic bulge and the nuclear stellar bulge, rather than a spherical excess. Given the non-spherical nature of our findings, we argue that the GCE is not a dark matter phenomenon but rather associated with the stellar population of the Galactic bulge and nuclear bulge.

The main challenge in pinning down the properties of the GCE is the correct modelling of diffuse Galactic emission from the interaction of cosmic rays with interstellar gas and radiation fields, by far the dominant source of gamma-rays in this sky region. The Fermi-LAT Collaboration designed a diffuse Galactic emission model based on a model-fitting template approach that is optimized to single out gamma-ray point sources (PSs) in the data[10]. This approach presupposes that the diffuse Galactic emission can be modelled as a linear combination of interstellar gas, inverse Compton (IC) maps, and several other diffuse components. Due to the limited kinematic resolution of gas tracers towards the GC, interstellar gas correlated gamma rays from the GC direction are particularly difficult to disentangle. Previous works[2–7,11] utilized interstellar gas maps that were constructed with an interpolation approach that assumes circular motion of interstellar gas in the inner few degrees of the GC. This kinematic assumption provides for an estimate of the distance to a given part of the interstellar gas. However, it is well established that the Galaxy contains a central bar which causes non-circular motion of interstellar gas in the inner Galaxy, so assuming circularity introduces a significant and avoidable bias to gamma-ray analyses of the GC region[12].

We use Fermi-LAT data accumulated between August 4, 2008 and September 4, 2015 in the $15^\circ \times 15^\circ$ region around the GC. State-of-the-art hydrodynamical simulations[12] that account for the dynamical effects of the Galactic bar were used to better determine the diffuse Galactic gamma-ray emissions. Gas maps informing the diffuse emission modelling were constructed by using a probabilistic deconvolution method for assigning gas clouds to distances via hydrodynamic gas flow model predictions. To critically evaluate the impact that the choice of interstellar gas models have on our results, we constructed atomic and molecular hydrogen gas maps using an interpolation approach that reproduced those used in most previous gamma-ray analyses of the GC. We split each into 4 concentric rings, each with its own normalization parameter. Full details of the model components and approach are provided in the Methods section.

Interstellar gas map templates constructed using the results of hydrodynamical simulations were found to be a better description of the diffuse gamma-ray data than the standard interpolation-based maps with a log likelihood ratio ≈ 1362. As we have additional data compared to that used to construct the Fermi-LAT 3FGL catalog[13], and more importantly since we also use a different galactic diffuse emission model, we searched for new point sources. We found 64 candidates (each with significance $\geq 4\sigma$) in our region of interest (ROI) which are shown as green crosses in Fig. 1. We find multi-wavelength counterparts for 18 of our 64 point source candidates. This is similar to the 3FGL catalogue[13] where some $\sim 1/3$ of the point sources do not have a multi-wavelength associations, especially in the GC region where there is high extinction and the diffuse Galactic emission model is more likely to require corrections. Given our point source candidates have high statistical significance, including them quantitatively affects our results; however, they do not qualitatively affect our conclusions (see the Systematic Errors subsection of the Methods).

Our canonical dark matter template for the GCE is modelled by the square of an Navarro-Frenk-White (NFW) template with an inner slope of 1.2). There is some tension with the dark matter interpretation and dwarf spheroidal observations, however when all the uncertainties are accounted for this does not definitively rule it out[16]. Extended gamma-ray emission in the GC may alternatively or additionally arise from unresolved sources. These can arise from millisecond pulsars (MSPs)[3,4] or young pulsars[8] both of which have GeV-peaked gamma-ray spectra. Recent studies have also shown detectable non-Poissonian features in photon statistics[17,18]. However, these may be due to defects in the Galactic emission mode[19]. The young pulsar hypothesis requires relatively recent star formation given the $\lesssim$ few Myr γ-ray lifetimes of ordinary pulsars. Such star formation is absent from most of the bulge except in the $r \lesssim 100$ pc nuclear region; a young pulsar explanation of the GCE thus requires that the bulge be populated with pulsars that are launched out of the nucleus. It has been claimed that this can be achieved naturally by the pulsar's natal kicks[8]. On the other hand, MSPs can be generated from old stellar populations[20].

We thus also consider Galactic bulge templates. Almost half the stars[21] in the Galactic bulge are on orbits that contribute to the appearance (from the Earth) of an X-shaped over-concentration (the 'X-bulge')[22]. This structure has been particularly clearly revealed in a recent analysis[14] of 3.4 and 4.6 micron data collected by the WISE telescope[23]. However, ref. 24 argued that the X-shape is a processing artefact. Our aim is *not* to scrutinize what is the correct bulge template,

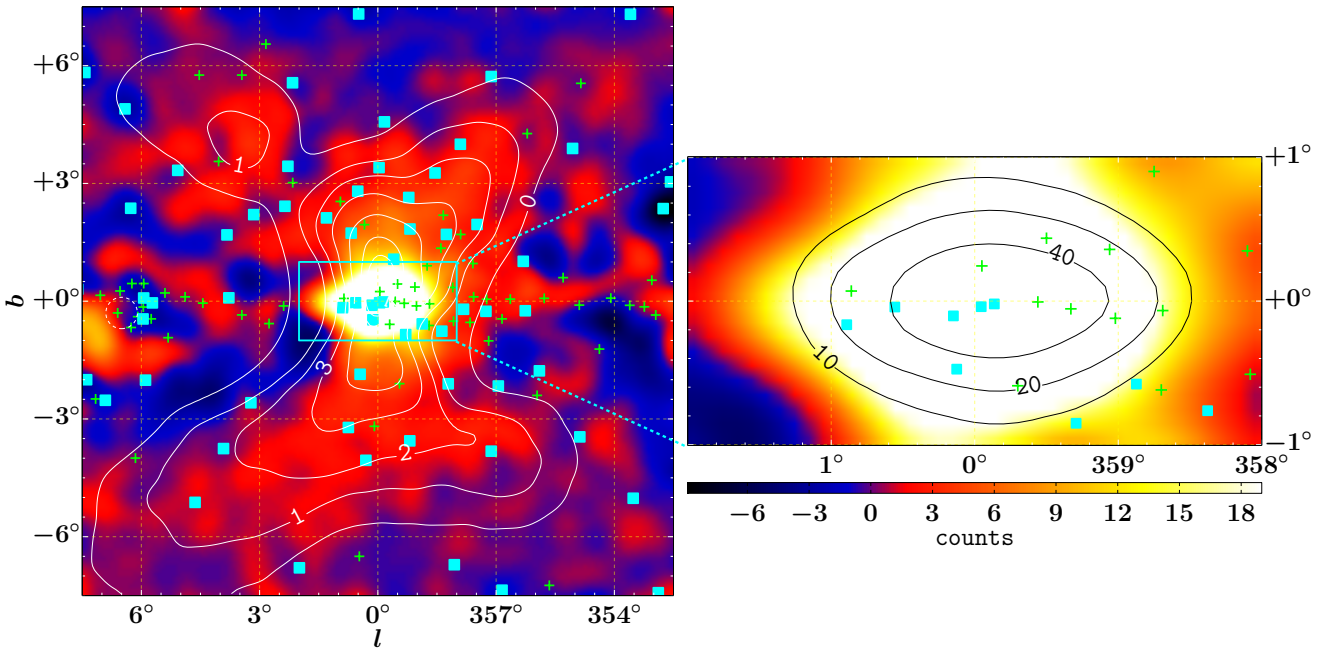

Figure 1: Residual map of the $15^\circ \times 15^\circ$ ROI for $E \geq 667$ MeV. The residuals are obtained as (Data − Model), where the model includes previously-detected 3FGL point sources (cyan squares)[13], 64 additional point source candidates (green crosses) and the standard diffuse Galactic emission components related to the interstellar gas and radiation field. The white contours are the best-fit model counts from the X-bulge map obtained from analyses of WISE[14] infrared data. The addition of a template based on the X-bulge improved the model fit to the gamma-ray data at the 16σ level. The cluster of point sources on the Galactic plane at $l \approx 6^\circ$ may be associated with the W28 (white dashed circle) supernova remnant[6,13]. The zoomed-in region on the right shows the correlation with the near-infrared stellar density nuclear bulge data[15], the black contours display the best-fit model counts associated to this component. The X-bulge and nuclear bulge templates were included when the best fit parameters for the above model were found, but not when evaluating the above residuals. A Gaussian with radius 0.3° was used to smooth the images for display purposes. The upper limit of the colour scale has also been clipped for display purposes.

but rather, to explore the bulge as an example astrophysical template for the GCE that is alternative to dark matter. Using standard maximum-likelihood estimation with a flux normalised X-bulge template based on the average of the 3.4 and 4.6 micron data, we find that the addition of our X-bulge template improves the fit to the gamma-ray data at about the 16σ level (see Table 1). This extends some earlier work[25] which found a significant improvement in the model fit with a 3.4 micron WISE based template in the inner 5 square degrees of the Fermi-LAT data, but which is not large enough to see the characteristic arms of the X.

A further distinct stellar component within the wider Galactic bulge is the so-called nuclear bulge. This disky distribution of stars concentrated within $\sim$ 230 pc radius of the Galactic nucleus has experienced on-going star formation over the life of the Galaxy and represents $\sim$ 10% of the overall bulge mass[26]. To determine whether the nuclear bulge template improves the fit to the Fermi-LAT gamma-ray data, we used a map constructed from a near-infrared stellar density measurement[15] and found a 10σ improvement in the fit (see Table 1). In Fig. 1 we show the residual gamma-ray map obtained after subtraction of our best-fit galactic diffuse emission and point sources model. Note that the fitting already included the X-bulge and nuclear bulge as proxy templates. This is a method required to avoid biasing the determination of the contribution from new extended components, see for example Fig. 3 of ref. 7. As can be seen, the X-bulge and nuclear bulge are well traced by our residual gamma-ray maps. The correlation with the X-bulge is more evident away from the plane where the hard-to-model diffuse Galactic emission is no longer so dominant. We have performed a $\pm 1^\circ$ mask of the plane, and found consistent results (see supplementary material).

Best-fit spectral parameters were found using χ^2 fitting to the inferred flux points for the energy bins. Relative to a power-law spec-

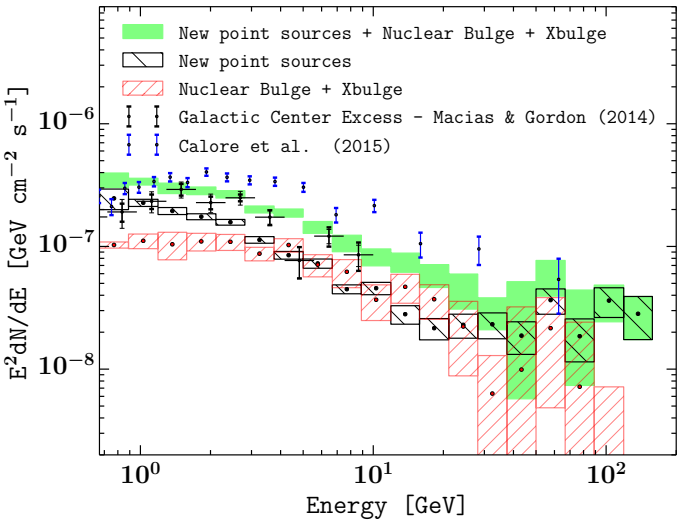

Figure 2: Differential flux of the new, statistically significant components in the Galactic centre. The black boxes are the combined spectrum of the 64 new point source candidates, red boxes are the superposition of the nuclear bulge and X-bulge differential fluxes, while the green boxes display the sum of these three components and are compatible with previous results[5,11], although, the comparison should only be taken as qualitative as the previous results are for slightly different ROI. The box sizes encompass the 68% confidence intervals. We found the combined nuclear bulge and X-bulge spectrum prefers an exponential cut-off to a power law model at 5σ.

trum, the preferred spectral model (at 3.5σ and 5.1σ respectively) for both the X-bulge and nuclear bulge templates was a power law with exponential cut-off (PLE:= $dN/dE \propto E^{-\Gamma}\exp(-E/E_{\rm cut})$). The X-bulge had a spectral slope of $\Gamma = 1.9 \pm 0.1$, an energy cut-off $E_{\rm cut} = 10 \pm 5$ GeV and a luminosity $L = (4.5 \pm 0.3) \times 10^{36}$ erg/s for $E \geq 100$ MeV. Similarly, the fit for the nuclear bulge yielded $\Gamma = 1.9 \pm 0.1$, $E_{\rm cut} = 13 \pm 4$ GeV and $L = (3.3 \pm 0.3) \times 10^{36}$ erg/s. Here and in the rest of the article 68% confidence intervals are used for error bars and we adopted 8.25 kpc for the distance to the GC. When the X-bulge and nuclear bulge spectra were combined (see Fig. 2), we found a PLE model was still preferred relative to a simple power law (PL:= $dN/dE \propto E^{-\alpha}$) model at 5.0σ. The best fit spectral parameters for this case are shown in Table 2. The combined X-bulge and nuclear bulge spectral parameters are compatible with previous estimates of the GCE based on templates of dark matter as well as resolved MSPs and globular clusters containing MSPs[11].

When the X-bulge and nuclear bulge templates are included in the fit, we find that a NFW template with an inner slope of 1.2 was not significantly detected (2σ, see Table 1). The 95% upper limit on this component's luminosity was found to be 5×10^{36} erg/s. Similarly, a dark matter template based on the square of an NFW profile with an inner slope of 1.0 was undetected.

The Fermi Bubbles[27,28] (FB) are giant lobes that extend up to ~ 7 kpc from the Galactic plane into both the North and South Galactic hemispheres. Recently, Acero et al.[10] performed a morphological study of these structures in the inner 20° of the GC. They found that the boundaries of the Fermi bubbles are well described by two catenary curves, see Methods section. However, the catenary geometry does not match the X-shaped excess we see in our residual and TS maps in Fig. 1 and Supplementary Fig. 5. We found the addition of a catenary template did not qualitatively affect our results. As this template had a low TS value (see Table 1) we did not include it in our final results but rather treated its potential presence as a systematic effect (see Table 2 and Methods section for further discussion).

In ref. 27, the spectrum of the Fermi bubbles was determined from the residuals in the energy range between 0.7 GeV and 10 GeV. They examined an area near the southern edge of the Fermi bubbles ($-55^\circ < b < -40^\circ$ and $-15^\circ < l < 15^\circ$). A power-law fit in this region had a spectral index index 1.9 ± 0.1. In contrast, we found our X-bulge and nuclear bulge, for the same energy range, had a power-law fit with a softer spectral index of 2.20 ± 0.05. Also, we estimate the X-bulge plus nuclear bulge has a solid angle of 0.03 sr, and therefore a luminosity per solid angle of $(1.0 \pm 0.1) \times 10^{38}$ erg/s/sr. By contrast, the Fermi bubbles, for $|b| \geq 10^\circ$, have a solid angle of about 0.7 sr and a luminosity[27] per solid angle of $(6.3 \pm 0.1) \times 10^{37}$ erg/s/sr. Even taking a wide range of systematic effects into account, the highest luminosity[27] per solid angle for the Fermi bubbles was only 8.6×10^{37} erg/s/sr.

ref. 7 used a spectral decomposition technique to determine the low latitude Fermi bubble contribution. However, their residuals for their GCE show the characteristic X-shape in their Fig. 3. Also, they found the addition of their Fermi bubbles template did not remove the need for an extra template to explain the GCE. In summary, current spatial and spectral evidence seems to disfavour a Fermi-bubbles explanation for all of the X-bulge and nuclear bulge emission.

A comparison between the properties of our proposed X-bulge and nuclear bulge MSPs with other MSP populations can be obtained by comparing the MSP luminosity to stellar mass ratio. Note that this comparison assumes the ratio of MSP mass to stellar mass is constant across the different considered regions which will only be approximately correct. The stellar mass[29] of the Galactic bulge is 1.5×10^{10} solar masses ($M_\odot$) and the nuclear bulge has a mass of $\sim 1.4 \times 10^9\ M_\odot$. According to ref. 21, instantaneous stellar mass contributing to the appearance of the X-bulge over-density represents about 25% of the Galactic bulge. However, as can be seen by comparing our Supplementary Fig. 6 to Fig. 18 of ref. 21, the method they use to determine this contribution underestimates the X-bulge we extract from the WISE data as it eliminates the central regions of the X-bulge that we have included in our template. Therefore, we estimate our X-bulge has an instantaneous stellar mass $\gtrsim 4 \times 10^9 M_\odot$. From these data we infer a $E \geq 100$ MeV luminosity-to-mass (LtM) ratio of $\lesssim 2 \times 10^{27}$ erg/s/$M_\odot$ for the combined X-bulge and nuclear bulge structure. This is similar to the LtM ratio we infer from ref. 30 for the MSP emission from the entire Milky Way of $\sim 2 \times 10^{27}$ erg/s/$M_\odot$ and somewhat less than the $\sim 5 \times 10^{28}$ erg/s/$M_\odot$ for globular cluster 47 Tuc[31] (which has an MSP-dominated > 100 MeV luminosity of $(4.8 \pm 1.1) \times 10^{34}$ erg/s and stellar mass of about $10^6 M_\odot$).

The upper limit derived from the NFW-squared template implies the rest of the bulge has a LtM ratio less than $\sim 8 \times 10^{26}$ erg/s/$M_\odot$. The region of the bulge outside the nucleus has experienced little star formation for many Gyr (and its stellar density is much lower than in globular clusters, limiting the potential for dynamical formation of close stellar binaries). Although subject to ongoing investigation, there are systematic differences between the stellar populations of the X and the bulge outside the X with stars in the X both higher in metallicity and likely systematically younger than other bulge stars, indeed, the spheroidal bulge population is likely one of the oldest in the Galaxy[29]. Given this, a relatively low LtM for the region outside the X is thus not unexpected given its MSPs are expected to be older (therefore slower spinning and less luminous) than the X region MSPs and MSPs found elsewhere in the Galaxy.

We have shown that the X-bulge and nuclear bulge provide a better fit than the dark matter explanation. We have not explicitly checked the burst model, but current implementations are highly model dependent and very fine-tuned[9]. Also, the young pulsar explanation is typically associated with spherically symmetric templates[8] and so also disfavoured compared to our MSP based X-bulge+nuclear bulge explanation. However, further observations will be needed to confirm that MSPS really are the sources of the GCE. One approach to do this will be to try and resolve the MSPs making up the X-bulge and nuclear bulge. It may be that many of the unassociated PSs in this region are already resolved MSPs and part of the GCE. Radio observations will likely be needed to confirm if these PSs are pulsating. Even if they are confirmed to be PSs, it will still be necessary to obtain more resolved PSs from future observations to determine whether the X-bulge+nuclear bulge templates are being traced to a statistically significant extent.

Table 1: Summary of the Likelihood analysis results

Base	Source	$\log(\mathcal{L}_{\rm Base})$	$\log(\mathcal{L}_{\rm Base+Source})$	$\rm TS_{Source}$	σ	Number of source parameters
baseline	FB	-172461.4	-172422.3	78	6.9	19
baseline	NFW-s	-172461.4	-172265.3	392	18.4	19
baseline	X-bulge	-172461.4	-172224.1	475	20.5	19
baseline	NFW	-172461.4	-172167.9	587	23.0	19
baseline	NB	-172461.4	-171991.8	939	29.5	19
baseline	NP	-172461.4	-169804.1	5315	55.7	64×19
baseline+NP	FB	-169804.1	-169773.6	61	5.8	19
baseline+NP	NB	-169804.1	-169697.2	214	13.0	19
baseline+NP	NFW	-169804.1	-169623.3	362	17.6	19
baseline+NP	X-bulge	-169804.1	-169616.2	376	18.0	19
baseline+NP+X-bulge	NFW	-169616.2	-169568.4	96	7.9	19
baseline+NP+X-bulge	NB	-169616.2	-169542.0	148	10.4	19
baseline+NP+X-bulge+NB	NFW	-169542.0	-169531.0	22	2.4	19
baseline+NP+X-bulge+NB	FB	-169542.0	-169525.5	33	3.5	19
baseline+NP+NB	X-bulge	-169697.2	-169542.0	310	16.1	19
baseline+NP+NFW	X-bulge+NB	-169623.3	-169531.0	185	10.8	2×19
baseline+NP+NFW+NB	X-bulge	-169598.9	-169531.0	136	9.9	19

The *baseline* model consists of all 3FGL point sources in the ROI, Loop I, an IC template predicted by GALPROP, the hydrodynamic based gas maps, the recommended isotropic emission map, and a model for the Sun and the Moon. Other model templates considered are: the 64 new point sources (NP), the square of a generalised NFW profile with an inner slope $\gamma = 1.2$ or the square of a "standard NFW" (NFW-s) with inner slope $\gamma = 1$, an infrared X-bulge template tracing old stars in the Galactic bulge, a nuclear bulge (NB) template and a template accounting for the Fermi Bubbles (FB). The maximized likelihoods ($\mathcal{L}$) are given for the Base and Base+Source models and the significance of the new source is given by $\rm TS_{Source} \equiv 2(\log(\mathcal{L}_{Base+Source}) - \log(\mathcal{L}_{Base}))$. Note that for both likelihoods all parameters are maximized and so the $\mathcal{L}_{\rm Base+Source}$ will have additional parameters whose number is given in the last column of the table. The conversion between $\rm TS_{Source}$ and σ is discussed in the Methods section.

Table 2: Exponential cut-off best-fit parameters with statistical and systematic errors to the X-bulge + nuclear bulge

Parameter	Best fit	Statistical Error	Systematic Error				
			Spin Temperature	Inverse Compton	Dust	Fermi Bubbles	Total
Γ	2.0	0.1	0.1	0.1	0	0.1	0.2
$E_{\rm cut}$/GeV	13	5	1	3	1	2	4
$L/(10^{36}{\rm erg/s})$	6	1	1	1	0	0	1

The statistical errors are 1σ. The total systematic error was obtained by adding in quadrature the individual systematic errors. Luminosities were computed for $E > 100$ MeV.

1. Atwood, W. B. *et al.* The Large Area Telescope on the Fermi Gamma-Ray Space Telescope Mission. *Astrophys. J.* **697**, 1071–1102 (2009). 0902.1089.
2. Goodenough, L. & Hooper, D. Possible Evidence For Dark Matter Annihilation In The Inner Milky Way From The Fermi Gamma Ray Space Telescope. *ArXiv e-prints (arXiv:0910.2998)* (2009). 0910.2998.
3. Abazajian, K. N. & Kaplinghat, M. Detection of a Gamma-Ray Source in the Galactic Center Consistent with Extended Emission from Dark Matter Annihilation and Concentrated Astrophysical Emission. *Phys. Rev.* **D86**, 083511 (2012). 1207.6047.
4. Gordon, C. & Macias, O. Dark Matter and Pulsar Model Constraints from Galactic Center Fermi-LAT Gamma Ray Observations. *Phys. Rev.* **D88**, 083521 (2013). 1306.5725.
5. Calore, F., Cholis, I. & Weniger, C. Background model systematics for the Fermi GeV excess. *J. Cosm. & Astropart. Phys.* **3**, 38 (2015). 1409.0042.
6. Ajello, M. *et al.* Fermi-LAT Observations of High-Energy γ-Ray Emission Toward the Galactic Center. *Astrophys. J.* **819**, 44 (2016). 1511.02938.
7. Ackermann, M. *et al.* The Fermi Galactic Center GeV Excess and Implications for Dark Matter. *Astrophys. J.* **840**, 43 (2017). 1704.03910.
8. O'Leary, R. M., Kistler, M. D., Kerr, M. & Dexter, J. Young Pulsars and the Galactic Center GeV Gamma-ray Excess. *ArXiv e-prints (arXiv:1504.02477)* (2015). 1504.02477.
9. Cholis, I. *et al.* The Galactic Center GeV excess from a series of leptonic cosmic-ray outbursts. *J. Cosm. & Astropart. Phys.* **12**, 005 (2015). 1506.05119.
10. Acero, F. *et al.* Development of the Model of Galactic Interstellar Emission for Standard Point-source Analysis of Fermi Large Area Telescope Data. *Astrophys. J. Supp.* **223**, 26 (2016). 1602.07246.
11. Macias, O. & Gordon, C. Contribution of cosmic rays interacting with molecular clouds to the Galactic Center gamma-ray excess. *Phys. Rev.* **D89**, 063515 (2014). 1312.6671.
12. Pohl, M., Englmaier, P. & Bissantz, N. Three-Dimensional Distribution of Molecular Gas in the Barred Milky Way. *Astrophys. J.* **677**, 283–291 (2008). 0712.4264.
13. Acero, F., Ackermann, M., Ajello, M., Albert, A. *et al.* Fermi Large Area Telescope Third Source Catalog. *Astrophys. J. Supp.* **218**, 23 (2015). 1501.02003.
14. Ness, M. & Lang, D. The X-shaped Bulge of the Milky Way Revealed by WISE. *Astrophys. J.* **152**, 14 (2016). 1603.00026.
15. Nishiyama, S. *et al.* Magnetically confined interstellar hot plasma in the nuclear bulge of our galaxy. *Astrophys. J. Lett.* **769**, L28 (2013). URL http://stacks.iop.org/2041-8205/769/i=2/a=L28.
16. Keeley, R., Abazajian, K., Kwa, A., Rodd, N. & Safdi, B. What the Milky Way's Dwarfs tell us about the Galactic Center extended excess (2017). 1710.03215.
17. Lee, S. K., Lisanti, M., Safdi, B. R., Slatyer, T. R. & Xue, W. Evidence for Unresolved γ -Ray Point Sources in the Inner Galaxy. *Phys. Rev. Lett.* **116**, 051103 (2016). 1506.05124.
18. Bartels, R., Krishnamurthy, S. & Weniger, C. Strong Support for the Millisecond Pulsar Origin of the Galactic Center GeV Excess. *Phys. Rev. Lett.* **116**, 051102 (2016). 1506.05104.
19. Horiuchi, S., Kaplinghat, M. & Kwa, A. Investigating the Uniformity of the Excess Gamma rays towards the Galactic Center Region. *JCAP* **1611**, 053 (2016). 1604.01402.
20. Ploeg, H., Gordon, C., Crocker, R. & Macias, O. Consistency Between the Luminosity Function of Resolved Millisecond Pulsars and the Galactic Center Excess (2017). 1705.00806.
21. Portail, M., Wegg, C. & Gerhard, O. Peanuts, brezels and bananas: food for thought on the orbital structure of the Galactic bulge. *Mon. Not. R. Astron. Soc.* **450**, L66–L70 (2015). 1503.07203.
22. Nataf, D. M., Udalski, A., Gould, A., Fouqué, P. & Stanek, K. Z. The Split Red Clump of the Galactic Bulge from OGLE-III. *Astrophys. J. Lett.* **721**, L28–L32 (2010). 1007.5065.
23. Wright, E. L. *et al.* The Wide-field Infrared Survey Explorer (WISE): Mission Description and Initial On-orbit Performance. *Astrophys. J.* **140**, 1868–1881 (2010). 1008.0031.
24. Joo, S.-J., Lee, Y.-W. & Chung, C. New Insight on the Origin of the Double Red Clump in the Milky Way Bulge. *Astrophys. J.* **840**, 98 (2017). 1609.01294.
25. Abazajian, K. N., Canac, N., Horiuchi, S., Kaplinghat, M. & Kwa, A. Discovery of a new galactic center excess consistent with upscattered starlight. *J. Cosm. & Astropart. Phys.* **7**, 13 (2015). 1410.6168.
26. Launhardt, R., Zylka, R. & Mezger, P. G. The nuclear bulge of the Galaxy. III. Large-scale physical characteristics of stars and interstellar matter. *Astron. Astrophys.* **384**, 112–139 (2002). astro-ph/0201294.
27. Ackermann, M. *et al.* The Spectrum and Morphology of the Fermi Bubbles. *Astrophys. J.* **793**, 64 (2014). 1407.7905.
28. Su, M., Slatyer, T. R. & Finkbeiner, D. P. Giant Gamma-ray Bubbles from Fermi-LAT: Active Galactic Nucleus Activity or Bipolar Galactic Wind? *Astrophys. J.* **724**, 1044–1082 (2010). 1005.5480.
29. Bland-Hawthorn, J. & Gerhard, O. The Galaxy in Context: Structural, Kinematic, and Integrated Properties. *Ann. Rev. Astron. Astrophys.* **54**, 529–596 (2016). 1602.07702.
30. Winter, M., Zaharijas, G., Bechtol, K. & Vandenbroucke, J. Estimating the GeV Emission of Millisecond Pulsars in Dwarf Spheroidal Galaxies. *ArXiv e-prints (arXiv:1607.06390)* (2016). 1607.06390.
31. Abdo, A. A. *et al.* A population of gamma-ray emitting globular clusters seen with the Fermi Large Area Telescope. *Astron. Astrophys.* **524**, A75 (2010). 1003.3588.
32. Strong, A. W. *et al.* Galprop version 54: Explanatory supplement. http://galprop.stanford.edu. Accessed: 2014-02-20.
33. Ackermann, M. *et al.* Fermi-lat observations of the diffuse gamma-ray emission: Implications for cosmic rays and the interstellar medium. *Astrophys. J.* **750**, 3 (2012). URL http://stacks.iop.org/0004-637X/750/i=1/a=3.
34. Kalberla, P. M. W. *et al.* The Leiden/Argentine/Bonn (LAB) Survey of Galactic HI. Final data release of the combined LDS and IAR surveys with improved stray-radiation corrections. *Astron. Astrophys.* **440**, 775–782 (2005). astro-ph/0504140.
35. Dame, T. M., Hartmann, D. & Thaddeus, P. The Milky Way in Molecular Clouds: A New Complete CO Survey. *Astrophys. J.* **547**, 792–813 (2001). astro-ph/0009217.
36. Delahaye, T., Fiasson, A., Pohl, M. & Salati, P. The GeV-TeV Galactic gamma-ray diffuse emission I. Uncertainties in the predictions of the hadronic component. *Astron. Astrophys.* **531**, A37 (2011). 1102.0744.
37. Schlegel, D. J., Finkbeiner, D. P. & Davis, M. Maps of Dust Infrared Emission for Use in Estimation of Reddening and Cosmic Microwave Background Radiation Foregrounds. *Astrophys. J.* **500**, 525–553 (1998). astro-ph/9710327.
38. Wolleben, M. A New Model for the Loop I (North Polar Spur) Region. *Astrophys. J.* **664**, 349–356 (2007). 0704.0276.
39. Johannesson, G., Orlando, E. & for the Fermi-LAT collaboration. Accounting for the Sun and the Moon in Fermi-LAT Analysis. *ArXiv e-prints (arXiv:1307.0197)* (2013). 1307.0197.
40. Nolan, P. L. *et al.* Fermi Large Area Telescope Second Source Catalog. *Astrophys. J. Supp.* **199**, 31 (2012). 1108.1435.
41. Mattox, J. *et al.* The Likelihood Analysis of EGRET Data. *Astrophys. J.* **461**, 396 (1996).
42. Wilks, S. S. The Large-Sample Distribution of the Likelihood Ratio for Testing Composite Hypotheses. *Ann. Math. Stat.* **9**, 60 (1938).
43. Yang, R.-Z. & Aharonian, F. On the GeV excess in the diffuse γ-ray emission towards the Galactic centre. *Astron. Astrophys.* **589**, A117 (2016). 1602.06764.
44. Manchester, R. N., Hobbs, G. B., Teoh, A. & Hobbs, M. The Australia Telescope National Facility Pulsar Catalogue. *Astron. J.* **129**, 1993–2006 (2005). astro-ph/0412641.
45. Harris, W. E. A Catalog of Parameters for Globular Clusters in the Milky Way. *Astron. J.* **112**, 1487 (1996).
46. Green, D. A. A catalogue of 294 Galactic supernova remnants. *Bull. Astron. Soc. India* **42**, 47–58 (2014). 1409.0637.
47. Massaro, E. *et al.* Roma-BZCAT: a multifrequency catalogue of blazars. *Astron. Astrophys.* **495**, 691–696 (2009). 0810.2206.
48. Fermi-LAT Collaboration. Characterizing the population of pulsars in the Galactic bulge with the $Fermi$ Large Area Telescope. *ArXiv e-prints* (2017). 1705.00009.
49. Hooper, D. & Linden, T. On The Origin Of The Gamma Rays From The Galactic Center. *Phys. Rev.* **D84**, 123005 (2011). 1110.0006.
50. Abazajian, K. N., Canac, N., Horiuchi, S. & Kaplinghat, M. Astrophysical and Dark Matter Interpretations of Extended Gamma-Ray Emission from the Galactic Center. *Phys. Rev.* **D90**, 023526 (2014). 1402.4090.
51. Daylan, T. *et al.* The characterization of the gamma-ray signal from the central Milky Way: A case for annihilating dark matter. *Phys. Dark Univ.* **12**, 1–23 (2016). 1402.6703.
52. Self, S. G. & Liang, K.-Y. Asymptotic properties of maximum likelihood estimators and likelihood ratio tests under nonstandard conditions. *Journal of the American Statistical Association* **82**, 605–610 (1987).
53. Casandjian, J.-M. Local H i Emissivity Measured with Fermi-LAT and Implications for Cosmic-Ray Spectra. *Astrophys. J.* **806**, 240 (2015). 1506.00047.
54. Chernoff, H. On the Distribution of the Likelihood Ratio. *The Annals of Mathematical Statistics* **25**, 573–578 (1954). URL http://links.jstor.org/sici?sici=0003-4851%28195409%2925%3A3%3C573%3AOTDOTL%3E2.0.CO%3B2-P.
55. Ackermann, M. *et al.* The Fermi Large Area Telescope On Orbit: Event Classification, Instrument Response Functions, and Calibration. *Astrophys. J. Supp.* **203**, 4 (2012). 1206.1896.

METHODS

Observations

We examined $\sim$ 7 years of Fermi-LAT data[1] (August 4, 2008−September 4, 2015) selecting PASS 8 ULTRACLEANVETO class events. The data was extracted from a square region of $15^\circ \times 15^\circ$ centred at Galactic coordinates $(l, b) = (0, 0)$ and made no distinction between *Front* and *Back* events. Furthermore, we restricted our analysis to the 667 MeV to 158 GeV energy range and used the P8R2_ULTRACLEANVETO_V6 instrument response functions. To avoid contamination from terrestrial Gamma-rays, we used events with zenith angles smaller than 90°. This work made use of the Fermi Science Tools `v10r0p5` software package.

Employing the `gtmktime` tool we selected the recommended data filters (DATA_QUAL>0)&&(LAT_CONFIG==1). Spatial binning was performed with the `gtbin` utility with which we divided the LAT data into 150×150 angular bins of size 0.1° in a `CAR` sky projection.

Templates

The Galactic diffuse gamma-rays resulting from the interaction of cosmic-ray electrons and protons with the interstellar gas and radiation field were modelled with a similar method used for the standard Galactic diffuse emission model[10]. We fitted a linear combination of atomic and molecular hydrogen gas templates, an IC energy-dependent spatial template as obtained with GALPROP[32], specialized templates for the *Sun* and the *Moon*, an isotropic component (`iso_P8R2_ULTRACLEANVETO_V6_v06.txt`), and a model for the gamma-ray emission associated with Loop I.

The atomic and molecular hydrogen gas column densities were each distributed within four Galactocentric annuli to account for the non-uniform cosmic-ray flux in the Galaxy. In the following subsections, we describe the construction of these templates.

We do not include the empirically-derived extended emission templates used by the Fermi-Collaboration when generating the publicly available version of the Galactic diffuse emission model provided for standard data analysis[10], because they were used to flatten residuals over larger regions of the sky than we are interested in this analysis and they are specifically constructed in support of the generation of the *Fermi*-LAT point-source catalogues.

HI and H_2 Gas Column Density Templates: We investigate two different methods for constructing the gas map templates:

1. Interpolation approach: this method has been used to produce the interstellar gas distribution models employed in most previous analyses of the GCE and is the standard approach employed in GALPROP and by the Fermi team.

   In the interpolation approach, the gas column density maps are produced using the method given in Appendix B of ref. 33. Atomic hydrogen column density is derived from the 21 cm LAB survey of Galactic HI[34]. Molecular hydrogen is traced by the 2.6 mm emission line of carbon monoxide (CO) from the 115 GHz centre for Astrophysics survey of CO[35]. The emission maps are decomposed into Galactocentric annuli via the relation,

   $$V_{\rm LSR} = \left(V(R)\frac{R_\odot}{R} - V(R_\odot) \right) \sin(l)\cos(b), \qquad (1)$$

   where $V_{\rm LSR}$ is the radial velocity, relative to the local standard of rest, of the gas at Galactocentric radius R with orbital velocity $V(R)$ observed in the direction (l, b) and $R_\odot$ is the distance of the Sun to the Galactic centre. We assumed a spin temperature of $T_S = 170\,{\rm K}$ throughout the Galaxy and $R_\odot = 8.25$ kpc. As in ref. 33, for CO, we assigned all high-velocity emission in the innermost annulus. For HI and the other CO annuli, the annuli decomposition interpolation method does not produce a reliable map of the gas column density as kinematic resolution is lost near $l = 0^\circ$. In the interpolation approach, the gas column density in the region $|l| < 10^\circ$ was estimated by interpolating within each annulus from the boundaries. Values at the boundaries of the interpolated region were chosen as the mean gas column density within a range of $\Delta l = 5^\circ$ on both sides of the boundary. Each pixel in the interpolated region was then renormalised to preserve the total gas column density in each line of sight.

2. Hydrodynamic approach: this method was pioneered by ref. 12. See also ref. 36 for discussion regarding the construction of the HI map. The presence of non-circular motion in the inner Galaxy provides kinematic resolution towards the GC. Outside the solar circle, pure circular motion with velocities described by equation (1), was assumed with an additional correction for the motion of the Sun relative to the local standard of rest. This meant there was lack of CO and HI gas placed in the outer annuli. We corrected for this by interpolating the outer annuli pixels in the line-of-sight maps which have $|l| < 15^\circ$ and then normalised each pixel to preserve the total gas column density in each line of sight. For CO we interpolated beyond 10 kpc and for HI we interpolated beyond 8 kpc from the GC.

The results of the two methods are compared in Supplementary Fig. 1. Note that in the interpolated approach, if the gas is placed above a certain height above the Galactic plane, it is assumed to be local[33]. This height differs between the gas distributions and was chosen to be 1 kpc for HI and 0.2 kpc for CO. This explains the high latitude CO gas difference in the 3.5–8.0 kpc and 8–10 kpc range of Supplementary Fig. 1. Somewhat broader radii were used in comparison to ref. 33 and 10 as we were fitting to a much smaller ROI and so the data we used had less constraining power and so broader annuli were needed.

Dust Correction Templates: Molecular hydrogen that is not well mixed with carbon monoxide will not be traced by the CO 2.6 mm emission. Furthermore, assuming a constant atomic hydrogen spin temperature $T_S = 170\,{\rm K}$ can give an incorrect estimate of column density as the spin temperature can vary along a line of sight. To correct for these deficiencies we included dust templates based on the methods used in ref. 33. Infrared thermal emission from dust provides an alternative method of tracing hydrogen gas in the Milky Way. The correction templates are obtained by subtracting the components of the dust emission that are correlated with the gas already traced by 21 cm and 2.6 mm emission.

We applied this method to $E(B-V)$ reddening maps[37]. Regions that are densely populated by infrared point sources (or potentially a collection of unresolved point sources) could contaminate the $E(B-V)$ reddening map, resulting in an over estimation of the dust column density. To mitigate this, we apply a magnitude cut of 5 mag and higher to the $E(B-V)$ reddening maps. After subtracting the components of the $E(B-V)$ map that were linearly correlated with the hydrogen gas maps, the residuals were separated into positive and negative components. The positive residuals physically represent hydrogen that is not traced by the relevant emission, known as the dark neutral medium, or an over estimation of the atomic hydrogen spin temperature. Negative residuals represent an underestimation of the spin temperature. The results are displayed in Supplementary Fig. 2.

Inverse Compton Emission Template: Whereas the bremsstrahlung and π^0-decay components can be adequately described by the gas maps described above, there is no analogous empirical template for the Galactic IC emission. We use the GALPROP package v54.1[32] to generate such a template. The authors of ref. 33 did a comprehensive comparison of 128 different GALPROP models with all sky Fermi-LAT data. They found a range of possible values for the input GALPROP parameters that are consistent with gamma-ray and local measurements of cosmic-ray data. In this work, we consider the IC template generated with GALDEF file `galdef_54_Lorimer_z10kpc_R20kpc_Ts150K_EBV2mag` as our reference model[33]. As seen from Supplementary Fig. 9, the IC component is of much smaller intensity compared to the interstellar gas diffuse Galactic emission components.

Loop I Template: Loop I is a bright, large angular scale, non-thermal structure. Obtaining a precise template of this source is not possible since its gamma-ray emission is not well traced by radio emission. Following the same approach taken in recent studies by the Fermi Collaboration[27],

in this work we used a geometrical template proposed by ref. 38 which is based on a polarization survey at 1.4 GHz (see Supplementary Fig. 3). We adopted the same morphological parameters for the shells assumed in ref. 27.

Sun and Moon emission Templates: In order to account for the diffuse emission from these objects, we construct specialized templates for our ROI by making use of the `gtsuntemp`[39] tool. The templates were constructed in Galactic coordinates with a Cartesian projection method. We note that the templates obtained with the use of this tool depend on the data selection. As such, we did not use the Sun and Moon templates that come with the 3FGL[13] as those were constructed for analysis of only 4 years of data.

Bin-by-Bin Analysis

Similar to other works[6,7], we employed a bin-by-bin analysis technique, in which we split the Fermi-LAT data into 19 logarithmically spaced energy bins. Within each energy bin we performed a separate maximum-likelihood fit[13] with the *pyLikelihood* analysis tool. The bin size was chosen to be larger than the LAT energy resolution, but narrow enough that the Galactic emission spectral components can be simply approximated by a power law model. We note that this bin-by-bin method enables us to evaluate the likelihood for a test source with an arbitrary spectral model and significantly reduces the CPU power required to reach convergence as only the flux normalization of the sources are free to vary during the fits.

Once the bin-by-bin method had converged, the inferred spectrum of each source was either fitted by a power law or an exponential cut-off model. When energy bins had $TS < 1$ or $\Delta F_i/F_i > 1$ they were combined with adjacent energy bins until $TS > 1$ and $\Delta F_i/F_i < 1$.

The errors from the bin-by-bin fit were added in quadrature to the errors caused by the uncertainties in the effective area[13]. These effective area errors were taken to be $f_i^{\rm rel}$ times the predicted flux for bin i. Where $f_i^{\rm rel}$ is interpolated from the values given in ref. 13. The spectrum was modelled by an exponential cut-off if

$$\mathrm{TS}_{\rm curvature} \equiv 2\left(\log \mathcal{L}(\text{exp. cut-off}) - \log \mathcal{L}(\text{power law})\right) \geq 9 \quad (2)$$

where $\mathcal{L}(i)$ is the maximum likelihood value for model i.

Comparing Hydrodynamic and Interpolated Gas Templates

Initially we fit the LAT data with a model comprised of the 3FGL[13] point sources present in our ROI plus four other spatially extended sources (HESS J1825-137, RX J1713.7-3946, W28 and W30) reported in the 3FGL[13]. The spatial templates used to model these extended sources correspond to Version 14.

To identify the most suitable gas templates for our study, we performed a scan in which we evaluated the improvement of the likelihood fit to the ROI when the gas maps used were the ones created with the interpolation method or the hydrodynamical method. Supplementary Fig. 4 shows that the data preferred the hydrodynamical method.

During optimisation, the flux normalisation of the 3FGL sources were left free in each energy bin. We also simultaneously fit the 13 diffuse components' (HI annuli, CO annuli, dust templates, Loop I, inverse Compton, and isotropic) normalisation but kept the *Sun* and *Moon* fluxes fixed to their nominal values.

Point Source Search

In order to check whether any additional PSs are required, we followed a methodology similar to that described in refs. 40 and 13. We started from our *baseline* model, which consists of all 3FGL point sources in the ROI, Loop I, an IC template predicted by GALPROP, the hydrodynamical based gas maps, the recommended isotropic emission map, and a model for the Sun and the Moon. We examined the significance of a trial point source with a power-law spectrum, with a fixed slope of two, at the centre of each pixel. The outcome of this was a residual TS map where the `gttsmap` utility was used for this step. In accordance with our bin-by-bin method, a residual TS map was computed for each energy bin and these were then added to get a total residual map for the full energy range.

From the total residual TS map we generated a list of all the pixel clusters with TS values above the detection threshold that looked reasonably isolated under visual inspection ($\sim 0.5^\circ$ of angular separation). The coordinates of the source candidates were calculated as the average of adjacent pixel positions weighted by their respective TS values[40]. A more sophisticated technique would be to fit the TS map with a two dimensional parabola. But, we found our results were not sensitive to the small difference in position that this gave. To avoid convergence issues, at each step we added only the ten (or fewer if less were available) brightest seeds to our model and reran the bin-by-bin analysis routine where *all* components $-$ including the new point sources $-$ were simultaneously fitted. Only the seeds that were found to have a TS above the detection threshold from this step were allowed to stay in the model. Note that this is an iterative procedure that goes from bright sources to faint ones. This procedure was repeated seven times in our ROI until no seeds were found or no more point source candidates passed the thresholding step. This made the method more robust against source confusion. When doing a global analysis, as opposed to a bin-by-bin analysis, each new point source candidate has two parameters for the power law and two parameters for its position. In that case a TS ≥ 25 (which corresponds to 4σ) is used as the detection condition[13,41]. However, since we used a bin-by-bin analysis with 19 energy bands in each of which the point source amplitude was not allowed to take on a negative value. As shown in the supplementary material, we thus have a mixture distribution given by

$$p(\mathrm{TS}) = 2^{-n}\left(\delta(\mathrm{TS}) + \sum_{i=1}^{n}\binom{n}{i}\chi^2_{i+2}(\mathrm{TS})\right) \quad (3)$$

where δ is the Dirac delta function, $\binom{19}{i}$ is a binomial coefficient, and χ^2_{i+2} is a χ^2 distribution with $i+2$ degrees of freedom. To work out the number of σ of a detection we evaluate the equivalent p-value for a one new parameter case[42]:

$$\text{Number of } \sigma \equiv \sqrt{\mathrm{InverseCDF}\left(\chi^2_1, \mathrm{CDF}\left[\mathrm{p(TS)}, \hat{\mathrm{TS}}\right]\right)} \quad (4)$$

where CDF and InverseCDF are the cumulative distribution and inverse cumulative distribution respectively. The first argument of each of these functions is the distribution function and the second is the value the CDF or InverseCDF is evaluated at. The observed TS value is denoted by $\hat{\mathrm{TS}}$. It follows that we use a threshold of TS ≥ 41.8 to correspond to a 4σ detection.

The total set of new point source candidates found in this work are displayed in Supplementary Fig. 5 along with the TS residual map obtained in our last iteration. Although the model including all the new point sources is a much better representation of the ROI, a few hot spots still remain. These are, however, found to be below the detection threshold of TS ≥ 41.8 in the maximum likelihood step. As can be seen from Supplementary Fig. 6, the X-bulge morphology is clearly visible in the residual TS values. Although, along the Galactic plane, in comparison to Fig. 2 and Supplementary Fig. 6, the X-bulge morphology is shifted to negative longitudes (a similar shift is seen in refs. 10, 43, and 7 with the use of different methods), this may be due to degeneracies between the X-bulge template and the amplitude of the 3FGL and new PSs around $l = 0, b = 0$. A similar phenomenon can be seen in Figs. 1 and 2 of ref. 4.

To identify possible multi-wavelength counterparts to the gamma-ray sources we searched in the seed locations within the 68% containment of the point spread function for one of our highest energy bands $\sim 0.1^\circ-$ around each source in the ATNF pulsar[44], globular cluster[45], supernova remnant (SNR)[46] and the Roma-BZCAT blazar[47] catalogues for potential gamma-ray emitters. We found spatial overlaps for 18 of our 64 point source candidates (see Supplementary Table 1). Note that this does not preclude the possibility that the other 46 point source candidates are real sources since high extinction towards the GC makes it difficult to have very complete multi-wavelength source catalogs.

Our new PSs are compared to the 2FIG[48] in Supplementary Fig. 7. As can be seen, there is a reasonable overlap considering that the two analyses used different diffuse galactic emission templates and that 2FIG was based on a wider energy range (0.3 to 500 GeV) and time interval (7.5 years). It is reassuring that the majority of new 2FIG sources that are not associated with one of our new PSs are on a hot spot of our TS map. The list of PSs found

in this work are provided as a FITS file in the online material to facilitate comparisons.

Including the 3FGL sources, we had a total of 109 point source candidates in our $|l| <= 7.5^\circ$, $|b| <= 7.5^\circ$ ROI. This is compatible with the 127 point source candidates found by ref. 7 for a disk like ROI with radius 10°.

New Templates

X-bulge: We followed a procedure based on the method described in ref. 14 applied to the WISE data. To use this template in comparisons with the Fermi-LAT data, all pixels values below zero were set to zero in each median filtered exponential subtracted map and our template was then constructed by taking the average of the two resultant maps. The resulting template is displayed in Supplementary Fig. 6.

Nuclear Bulge: We used a map constructed from a near-infrared stellar density measurement of the central region of our Galaxy ($|l| \geq 3^\circ$ and $|b| \geq 1^\circ$) and subtracted a best fit Galactic disk component[15]. In order to remove artificial sharp boundaries in the map induced by survey patches, all pixels below 15 stars/arcmin^2 were set to zero. The resulting template is displayed in Supplementary Fig. 8.

Dark Matter: We modelled the potential annihilating dark matter signal in the GC as the square of an NFW density profile with an inner slope of 1.2, which had been shown to describe the GCE well in previous works[2–7,11,49–51]. The square of an NFW density profile is representative of a tentative annihilating dark matter signal in the GC.

Fermi Bubbles: As found by Acero et al.[10], we use two catenary curves of the form $10.5^\circ \times (\cosh((l-1^\circ)/10.5^\circ) - 1^\circ)$ and $8.7^\circ \times (\cosh((l+1.7^\circ)/8.7^\circ) - 1^\circ)$ for the Northern and the Southern bubbles, respectively.

Testing Extended Emission Templates

We fitted the gamma-ray emission with our bin-by-bin method to derive fluxes that are independent of the choice of spectral model. Within each bin, the spectrum of the included point and extended sources were modelled as power laws with fixed spectral index of two. Due to the small size of the bins, our results were not sensitive to the precise spectral index used. In each energy bin, the amplitudes of all included point sources and all included extended templates were simultaneously fit. This allowed us to effectively marginalise over the statistical uncertainties. Table 1 shows the steps we took to evaluate whether a template was significantly detected. We started with the *baseline* model and then evaluated the TS of each new template. We then added the template with the highest TS to our model and repeated the procedure with this appended to the Base model. We iterated through these steps until the highest TS-value of a new template was below our 4σ threshold. For each new template there are $n \times 19$ new parameters.The probability distribution is the same as equation (3) except that the 19 should be replaced by $n \times 19$ and the χ^2_{i+2} should be replaced with χ^2_i as we are not fitting the positions of the template. This is the same formula as in case 9 of ref. 52. For one new template being considered (i.e. 19 new parameters), our 4σ detection threshold corresponded to $TS \geq 38.4$.

The contributions of the different components for our proposed model of the GCE are shown in Supplementary Fig. 9. The fractional residuals are shown in Supplementary Fig. 10. As can be seen from the top left panel, the X-bulge is needed even when the interpolated gas maps are used. Comparing the top and bottom right panels shows that the X-bulge morphology has been accounted for by our template.

Molecular-Hydrogen-To-CO Conversion Factor

Our inferred molecular-hydrogen-to-CO conversion factor (X_{CO}) is shown in Supplementary Table 2. As in ref. 10 we evaluated X_{CO} using our 2 GeV energy bin fit results. Our values are consistent with the results from all sky fits as can be seen from comparing to Fig. 25 of ref. 33. Although our 8 to 10 kpc best fit X_{CO} is somewhat larger than the all sky and high latitude[53] measurements, it does also have large error bars and so is still consistent with the other measurements at about 2σ or better level even when only statistical errors are accounted for. As in ref. 33, our X_{CO} values for the outer annuli were strongly biased because the model under-fitted the data in the outer galaxy and so we do not report them.

We found most of our results were not sensitive to changing the number of annuli to five. This was done by splitting our first annuli into two annuli with radii 0 to 1.5 kpc and 1.5 to 3.5 kpc as in ref. 7. However, we got unrealistic X_{CO} values for the innermost annuli in that case. Therefore, we stuck to the four annuli case shown in Supplementary Fig. 1. Note that we did not explicitly use the X_{CO} values in performing our fits and we are only quoting their inferred values to demonstrate the fitted amplitudes for our interstellar gas maps are reasonably consistent with previous results.

Systematic Errors

Our analysis involved making choices for the spin temperature, the cosmic-ray source distribution, the $E(B-V)$ reddening map magnitude cut, and also whether or not to include a template for the Fermi bubbles. We evaluate the associated systematic errors by seeing how the best fit exponential cut-off parameters change when different choices were made. To do this for the spin temperature, we used $T_S = 150$ K instead of $T_S = 170$ K. For the IC model we changed the cosmic ray source distribution from "Lorimer" to "OBstars"[33] as this was found to have the greatest effect on the IC morphology. We found changing other parameters for the IC model had negligible effects. The dust systematic error was evaluated by changing the $E(B-V)$ reddening map magnitude cut from 5 mag and above to 2 mag and above. The Fermi bubbles systematic error was obtained by including the catenary template in the fit. The resulting systematic errors are given in Table 2.

We also checked the sensitivity of our results to the background model and new point sources. As can be seen from Supplementary Table 3, the Xbulge+nuclear bulge are still needed by the data when no new point sources are included, or when the interpolated gas maps are used, or when the 2FIG point sources are used. The NFW was still needed by the data, after the X-bulge and nuclear bulge were included, only in the case of the interpolated gas maps.

To evaluate the impact that potential mismodeling of the Galactic plane could have in our main results we masked the inner $|b| < 1^\circ$ of the ROI (see Supplementary Fig. 11) and utilized a statistical procedure similar to that in Table 1. We used the `Composite2` tool within the *Fermi* Science Tools and performed a composite likelihood analysis of the unmasked ROIs simultaneously for each energy bin (this method was first used in the GC region in ref. 19). We tied across the regions $b > 1^\circ$ and $b < -1^\circ$ of the inner $15^\circ \times 15^\circ$ of the GC and constrained the normalization of all the extended templates to be the same throughout the two separate ROIs at each energy bin. The majority of the new point sources as well as the nuclear bulge template reside in the $|b| < 1^\circ$ region, so this analysis pipeline considered the 22 new point sources outside the masked region, the X-bulge and the NFW templates in an attempt to model the GCE. The results are shown in Table 4. As it can be seen, the data still significantly favours an X-bulge template over a spherical template.

As an additional check, we also evaluated the correlation matrix around our best fit model. We found that the correlation coefficients between all extended components and our X-bulge and nuclear bulge templates were in the range 10^{-10} to 10^{-2} in all energy bins. With such small correlations even systematic biases in the templates several times larger than the statistical uncertainties would not substantially affect the fitted normalizations of the two bulge templates. Further sources of systematic errors may arise from the choices made in constructing the X-bulge and nuclear bulge templates. We will investigate these in future work.

Materials & Correspondence Correspondence and requests for materials should be addressed to Oscar Macias. (email: oscar.macias@vt.edu).

Acknowledgements RMC was the recipient of an Australian Research Council Future Fellowship (FT110100108). We thank Dustin Lang for making available code and data which helped with generating the X-bulge template and both Shogo Nishiyama and Kazuki Yasui for providing the data for the Nuclear bulge template. We acknowledge the use of public data and software

from the Fermi data archives (http://fermi.gsfc.nasa.gov/ssc/). Finally, the authors would also like to thank Felix Aharonian, Anthony M. Brown, Francesca Calore, Jean-Marc Casandjian, H. Thankful Cromartie, Seth Digel, Torsten Enßlin, Manoj Kaplinghat, Ken Freeman, Ortwin Gerhard, Oleg Gnedin, Xiaoyuan Huang, Naomi McClure-Griffiths, David Nataf, Ben Roberts, Miles Winter, Richard Tuffs, and Gabrijela Zaharijas for enlightening discussions.

Author contributions OM designed and performed the majority of the data analysis. OM also constructed the Fermi Bubbles, Sun, Moon, Inverse Compton and Loop I templates. CG processed the WISE data. RMC suggested the link with the X-bulge. BC processed the hydrodynamical 3D map into annuli density maps. DP created the interpolated annuli density maps. CG and SH assisted with the PS modelling. BC and DP created the dust maps. MP created the three dimensional HI and CO maps. All authors contributed to the interpretation of the results. OM and CG contributed mainly to the the text of the final manuscript, but all authors did have some contribution.

Competing Interests The authors declare that they have no competing financial interests.

Supplementary Information

Mixture Distributions

Wilks' theorem states that the asymptotic distribution of TS is given by Chi squared distribution (χ^2_q) where q is the number of new parameters. This can be used to evaluate a p-value $[1 - p(\mathrm{TS} > \mathrm{TS}_{\mathrm{thresh}})]$ of some threshold value of TS above which the new parameters are accepted as being statistical significant. However, this theorem does not hold if any of the null values of the new parameters are on the boundary of the allowed parameter space. This is problematic for when one wants to decide whether there is a new source in the data which can only have a non-negative amplitude. This limitation can be alleviated using the Chernoff theorem[54] which implies that if the new parameter is the proposed source's amplitude then the TS distribution will be given by a mixture distribution:

$$p(\mathrm{TS}) = \frac{1}{2}(\delta(\mathrm{TS}) + \chi^2_1(\mathrm{TS})). \tag{5}$$

where δ is the Dirac delta function. This formula just states that under the null hypothesis, half the time the evaluated amplitude will be negative (in which case TS is assigned) and the other half of the time (when the amplitude is non-negative) the distribution will follow from Wilks' theorem. This method was shown to work well for simulations of EGRET data by ref. 41. They also proposed that an extension which includes parameters for the two dimensional position of the source has a distribution of

$$p(\mathrm{TS}) = \frac{1}{2}(\delta(\mathrm{TS}) + \chi^2_3(\mathrm{TS})) \tag{6}$$

which they checked is correct by comparing to simulated EGRET data. In some cases sources are found to significantly prefer a curved spectrum[13]. For example, pulsars generally have an exponential cut-off spectrum. Therefore, it may be preferable to test for some new source with a non-parametric spectrum so as not too cause any bias by using a spectrum different from the spectrum the source has. This can be done by doing a bin by bin analysis where the energy range is broken up into a number of bins. If the bins are made sufficiently small, then a power law with Γ set to some fixed value (such as 2) can be used in each bin without loss of generality. Although, the bins shouldn't be too small otherwise one starts to get correlations between the different energy bins due to the finite energy dispersion of the Fermi-LAT instrument[55]. For the case of a testing for a new source at a fixed position we can use $\mathrm{TS} = \sum_{i=1}^{n} \mathrm{TS}_i$ where TS_i is the TS for bin i and there are n bins. We can then utilize the formula given in case 9 of ref. 52:

$$p(\mathrm{TS}) = 2^{-n}\left(\delta(\mathrm{TS}) + \sum_{i=1}^{n}\binom{n}{i}\chi^2_i(\mathrm{TS})\right) \tag{7}$$

where the amplitude in each energy bin needs to be non-negative. This equation has a simple interpretation in terms of mixture distributions. The 2^{-n} term is equal to the number of distinct ways n bins could have a non-negative or negative best fit amplitude. As there is only one way they could all have a negative amplitude, that is the weight of the δ function. While if the there are i non-negative amplitudes they would have $\binom{N}{i}$ distinct configurations and each of these configurations would have a χ^2_i distribution. As discussed in the Methods section, we used equation (7) in testing for new extended sources.

When testing for new PSs, the two position variables of the proposed new point source should also be included. They are not on the boundary of the allowed range under the null hypothesis. Case 9 of ref. 52 also covers the case where n of the new variable are restricted and two are not:

$$p(\mathrm{TS}) = 2^{-n}\left(\sum_{i=0}^{n}\binom{n}{i}\chi^2_{i+2}(\mathrm{TS})\right). \tag{8}$$

However, this formula is not quite the one we are looking for as when all the bins have non-positive best fit amplitudes, we need to have $\mathrm{TS} = 0$ regardless of the values of the position variables. Therefore, in order to modify equation (8) for our case of interest, we need to subtract off $2^{-n}\binom{N}{0}\chi^2_2 = 2^{-n}\chi^2_2$ and add on a $2^{-n}\delta(\mathrm{TS})$ term. This gives equation (3) of the Methods section.

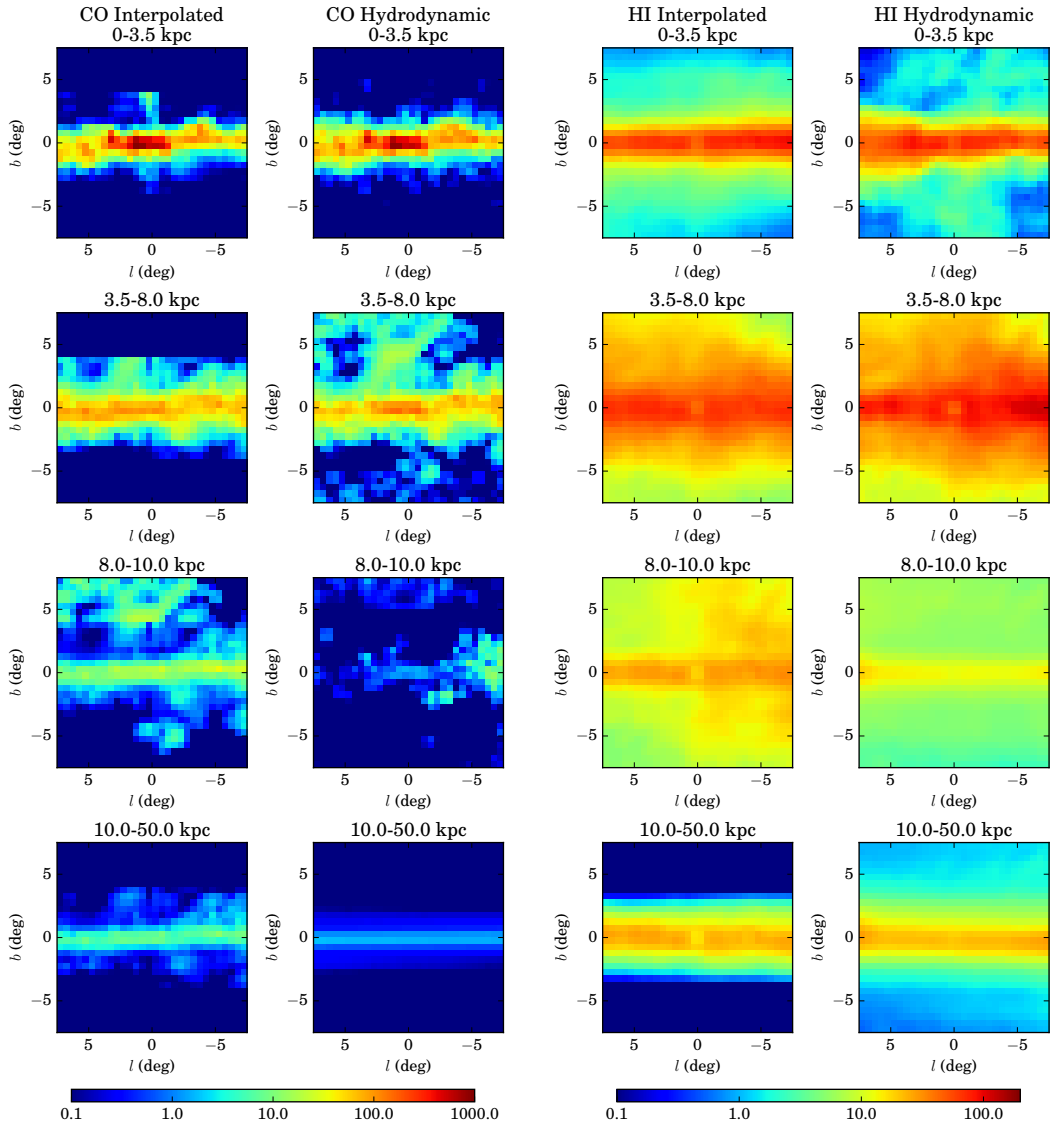

Supplementary Figure 1: Column density maps for the interpolated and hydrodynamic methods. The minimum and maximum radii of each annulus is listed. The units for the H_2 proportional CO maps are K·km/s. The units for the HI maps are $10^{20}\mathrm{cm}^{-2}$.

Supplementary Table 1: Point Sources detected with $TS \geq 41.8$ for the $15^\circ \times 15^\circ$ region about the Galactic Center.

Name	l [deg]	b [deg]	Association or spatial overlap	TS	$F_{1-100\,\mathrm{GeV}}$ $\times 10^{-9}$ [ph cm^{-2} s^{-1}]	Spectrum
FGC 1711.3 -3008	354.9	5.6	2FIG J1711.0-3005	78.2	2.5 ± 0.3	1.9 ± 0.2
FGC 1719.7 -2947	356.2	4.3	2FIG J1719.1-2945	47.7	1.9 ± 0.3	2.2 ± 0.4
FGC 1725.9 -3429	353.1	0.5		55.7	5.7 ± 0.8	2.6 ± 0.2
FGC 1727.7 -2302	2.8	6.6	2FIG J1727.7-2305	71.5	1.3 ± 0.2	1.9 ± 0.1
FGC 1729.1 -3443	353.2	-0.1	1FIGJ1728.6-3433	109.2	5.4 ± 3.4	2.7 ± 0.3
FGC 1729.2 -3504	353.0	-0.4	2FIG J1729.1-3501, 1FIGJ1729.1-3502	52.7	2.6 ± 16.9	1.9 ± 0.4
FGC 1729.9 -3423	353.6	-0.1	2FIG J1730.0-3421	57.2	4.9 ± 0.9	2.7 ± 2.8
FGC 1730.5 -3353	354.1	0.1	2FIG J1730.8-3356, 1FIGJ1730.2-3351, G354.1+0.1 [46], PSR J1730-3350 [44]	113.2	9.8 ± 0.8	3.2 ± 0.2
FGC 1731.6 -3235	355.3	0.6	2FIG J1731.3-3235, 1FIGJ1731.3-3235,	143.3	15.1 ± 0.8	0.0 ± 0.0

Continued on next page

Supplementary Table 1 – continued from previous page

Name	l [deg]	b [deg]	Association or spatial overlap	TS	$F_{1-100\,\mathrm{GeV}}$ $\times 10^{-9}$ [ph cm^{-2} s^{-1}]	Spectrum
			G355.4+0.7 [46]			
FGC 1732.1 -2257	3.5	5.8	2FIG J1731.3-2303	49.6	1.7 ± 0.3	2.3 ± 0.7
FGC 1733.1 -2910	358.3	2.2	2FIG J1732.6-2901	71.3	3.4 ± 0.5	2.2 ± 0.4
FGC 1733.3 -3318	354.9	-0.1	Liller 1 [45]	57.4	4.6 ± 0.8	2.8 ± 0.2
FGC 1733.9 -2948	357.9	1.7		55.8	1.3 ± 0.4	2.3 ± 0.2
FGC 1734.6 -2202	4.5	5.8		73.7	2.1 ± 0.3	1.9 ± 0.5
FGC 1734.9 -3228	355.8	0.1	2FIG J1734.6-3237, 1FIGJ1734.6-3228, G355.60.0 [46]	91.3	8.8 ± 0.8	2.6 ± 0.3
FGC 1735.1 -3028	357.6	1.0	2FIG J1735.7-3025, 1FIGJ1735.4-3030, Terzan 1 [45]	163.3	8.0 ± 0.7	$1.9 \pm 0.2,\ 5.9 \pm 1.3$
FGC 1736.5 -2934	358.4	1.4		44.2	3.3 ± 0.6	2.4 ± 0.2
FGC 1736.5 -3420	354.4	-1.2	2FIG J1736.2-3422, 1FIGJ1736.1-3422	101.9	3.3 ± 0.5	$1.9 \pm 0.1,\ 5.7 \pm 1.1$
FGC 1737.2 -3145	356.6	0.1	1FIGJ1737.4-3144	177.7	12.0 ± 0.9	2.4 ± 0.4
FGC 1738.1 -2647	1.0	2.5	PSR J1801-2451 [44]	43.1	1.7 ± 0.5	2.4 ± 0.6
FGC 1738.7 -3115	357.2	0.1		49.6	3.3 ± 0.9	2.0 ± 1.8
FGC 1738.9 -2737	0.3	2.0		50.4	1.7 ± 0.5	2.1 ± 0.7
FGC 1739.1 -2931	358.8	0.9		84.5	5.1 ± 0.7	1.9 ± 0.4
FGC 1739.2 -2530	2.2	3.0		56.2	2.7 ± 0.5	2.3 ± 0.4
FGC 1739.3 -3056	357.6	0.1	1FIGJ1740.1-3057	111.3	9.5 ± 1.0	2.6 ± 0.4
FGC 1739.6 -3022	358.1	0.4	1FIGJ1739.4-3010, PSR J1739-3023 [44]	363.3	12.5 ± 0.9	1.9 ± 2.3
FGC 1739.7 -3151	356.9	-0.5		48.0	2.9 ± 0.8	2.9 ± 0.5
FGC 1741.1 -2932	359.1	0.4		50.0	3.0 ± 1.1	2.0 ± 0.9
FGC 1741.5 -2337	4.0	3.6		50.3	2.2 ± 1.7	$1.9 \pm 0.6,\ 1.5 \pm 0.3$
FGC 1742.1 -3050	358.1	-0.5		66.3	5.6 ± 1.0	2.7 ± 0.2
FGC 1742.1 -3112	357.7	-0.5		46.7	3.0 ± 0.8	$1.9 \pm 0.2,\ 1.8 \pm 0.2$
FGC 1742.7 -2907	359.5	0.4	2FIG J1742.3-2916	90.4	4.7 ± 1.2	2.4 ± 0.8
FGC 1742.7 -3005	358.7	-0.1		161.2	5.4 ± 1.2	1.9 ± 2.4
FGC 1742.8 -3151	357.2	-1.0	G00.9+00.1 [46], PSR J1747-2809 [44]	49.8	1.9 ± 0.6	2.2 ± 0.3
FGC 1743.7 -2950	359.0	-0.1		56.8	7.9 ± 1.4	3.5 ± 0.5
FGC 1744.2 -2932	359.3	-0.1	2FIG J1744.2-2921, 1FIGJ1744.2-2930	391.7	2.1 ± 1.9	1.9 ± 1.4
FGC 1744.5 -2851	360.0	0.2		65.7	5.1 ± 1.7	2.6 ± 0.7
FGC 1744.6 -2918	359.6	0.0	2FIG J1744.2-2921	84.5	1.4 ± 1.8	1.9 ± 0.2
FGC 1744.9 -3022	358.7	-0.6	2FIG J1744.1-3024, 2FIG J1744.6-3011, 2FIG J1745.7-3023	52.0	4.6 ± 1.4	1.9 ± 0.2
FGC 1745.4 -3338	356.0	-2.4	2FIG J1745.9-3341, G355.92.5 [46]	43.0	2.3 ± 0.4	2.4 ± 0.4
FGC 1747.2 -2929	359.7	-0.6	2FIG J1746.5-2926	44.9	4.3 ± 1.2	1.9 ± 2.2
FGC 1747.4 -2809	0.9	0.1	2FIG J1747.1-2813, G0.9+0.1 [46], PSR J1747-2809 [44]	56.0	10.3 ± 1.5	2.7 ± 0.1
FGC 1751.7 -2657	2.4	-0.1		101.1	6.4 ± 0.8	3.1 ± 0.3
FGC 1752.6 -3029	359.5	-2.1		62.8	1.1 ± 0.3	1.9 ± 2.0
FGC 1754.1 -2609	3.5	-0.4		72.9	5.3 ± 0.8	1.9 ± 2.0
FGC 1754.2 -2651	2.8	-0.6		45.2	1.6 ± 0.7	2.0 ± 1.8
FGC 1756.0 -2508	4.4	0.0	2FIG J1756.0-2515, 1FIGJ1755.5-2511	225.5	9.8 ± 0.9	2.1 ± 0.9
FGC 1756.4 -2440	4.9	0.1	2FIG J1756.7-2433	59.7	5.2 ± 0.8	2.5 ± 0.2
FGC 1757.2 -2411	5.4	0.2	2FIG J1757.6-2414, G5.5+0.3 [46]	59.7	3.7 ± 0.7	2.1 ± 0.4
FGC 1757.4 -2335	5.9	0.5	G6.1+0.5 [46]	47.1	0.5 ± 0.2	1.9 ± 1.6

Continued on next page

Supplementary Table 1 – continued from previous page

Name	l [deg]	b [deg]	Association or spatial overlap	TS	$F_{1-100\,\mathrm{GeV}}$ $\times 10^{-9}$ [ph cm^{-2} s^{-1}]	Spectrum
FGC 1758.1 -2320	6.2	0.5	G6.1+0.5 [46]	59.7	1.8 ± 0.6	4.1 ± 0.5
FGC 1758.5 -3028	0.1	-3.2	2FIG J1758.3-3027, NGC 6569 [45]	63.9	1.4 ± 0.3	2.0 ± 0.5
FGC 1759.5 -2310	6.5	0.3	2FIG J1759.2-2313, PSR J1759-2307 [44]	55.0	2.3 ± 1.1	1.9 ± 2.2
FGC 1759.7 -2353	6.0	-0.2	2FIG J1759.6-2352	100.4	2.9 ± 1.5	2.0 ± 2.6
FGC 1800.1 -2247	7.0	0.2	2FIG J1801.7-2244, G7.2+0.2 [46]	46.8	10.2 ± 0.9	3.0 ± 0.2
FGC 1800.1 -2353	6.1	-0.4		54.6	5.9 ± 1.8	2.1 ± 0.4
FGC J1800.4 -2412	5.8	-0.5		45.7	0.2 ± 0.5	2.8 ± 2.0
FGC 1801.3 -2449	5.3	-0.9	2FIG J1801.5-2450, 1FIGJ1801.2-2451, PSR J1801-2451 [44]	124.4	10.5 ± 0.7	2.5 ± 0.2
FGC 1801.7 -2324	6.6	-0.3	1FIGJ1801.4-2330, G6.50.4 [46]	131.2	55.2 ± 1.5	$2.4 \pm 0.1,\ 9.8 \pm 4.9$
FGC 1802.4 -2352	6.3	-0.7	2FIG J1801.9-2359, 1FIGJ1801.6-2358	77.0	4.8 ± 1.2	2.6 ± 0.3
FGC 1805.1 -3619	355.7	-7.2	2FIG J1805.0-3620	64.9	1.7 ± 0.2	$1.9 \pm 0.1,\ 1.7 \pm 0.2$
FGC 1811.2 -2358	7.2	-2.5	2FIG J1811.3-2403	53.4	1.9 ± 0.5	1.9 ± 1.9
FGC 1812.9 -3145	0.5	-6.5	2FIG J1813.0-3144	61.7	1.7 ± 0.2	2.0 ± 0.2
FGC 1814.1 -2535	6.2	-4.0		41.8	1.2 ± 0.3	1.9 ± 2.1

This table is also provided as a FITS file in the supplementary online material. The third column displays 1FIG[6] and 2FIG[48] associations as well as spatial overlaps with tentative multi-wavelength counterparts. We use the globular cluster catalog[45], ATNF pulsar catalog[44], Green's SNR catalog[46], and the Roma-BZCAT blazar catalog[47]. Best-fit fluxes were obtained in the $1 - 100$ GeV energy range are denoted by $F_{1-100\,\mathrm{GeV}}$. The spectrum column gives the spectral slope for a power law fit, except in the case where an exponential cutoff model was preferred at $\geq 4\sigma$ level where the E_{cut} in GeV units is also given. Similarly to ref. 13, we combined our energy bands into four larger bands before fitting the spectrum. The errors are 1σ.

Supplementary Table 2: Radial distribution of X_{CO} as obtained from our maximum likelihood estimation using the hydrodynamic gas template models.

Annulus	$0 - 3.5$ kpc	$3.5 - 8.0$ kpc	$8.0 - 10.0$ kpc
X_{CO}	0.4 ± 0.1	1.0 ± 0.2	3.9 ± 1.3

The quoted values are for the first three annuli and are in units of $10^{20}[\,\mathrm{cm}^{-2}\,(\mathrm{K\ km\ s}^{-1})^{-1}]$. The errors are 1σ.

Supplementary Table 3: Systematic likelihood analysis results

Base	Source	$\log(\mathcal{L}_{\mathrm{Base}})$	$\log(\mathcal{L}_{\mathrm{Base+Source}})$	$\mathrm{TS}_{\mathrm{Source}}$	σ	Number of source parameters
baseline+NB+X-bulge	NFW	-171956.4	-171948.7	15	1.5	19
baseline+NFW	NB+X-bulge	-172167.9	-171948.7	438	18.6	2×19
baseline*	NFW	-173565.0	-172929.2	1272	34.6	19
baseline*+NFW	NB+X-bulge	-172929.2	-172592.0	674	23.8	2×19
baseline*+NB+X-bulge	NFW	-172631.5	-172592.0	79	6.9	19
baseline	2FIG	-172461.4	-170710.5	3501	37.3	81×19
baseline+2FIG	X-bulge	-170710.5	-170487.3	446	19.8	19
baseline+2FIG	NFW	-170710.5	-170484.6	452	19.9	19
baseline+2FIG	NB	-170710.5	-170470.5	480	20.6	19
baseline+2FIG+NB	NFW	-170470.5	-170387.8	165	11.1	19
baseline+2FIG+NB	X-bulge	-170470.5	-170307.6	326	16.6	19
baseline+2FIG+NB+Xbulge	NFW	-170307.6	-170301.8	12	1.1	19

See the caption of Table 1 for definitions. The *baseline** is same as the *baseline* model, except that it uses the interpolated gas maps. 2FIG are the 81 new point sources found in our ROI by ref. 48.

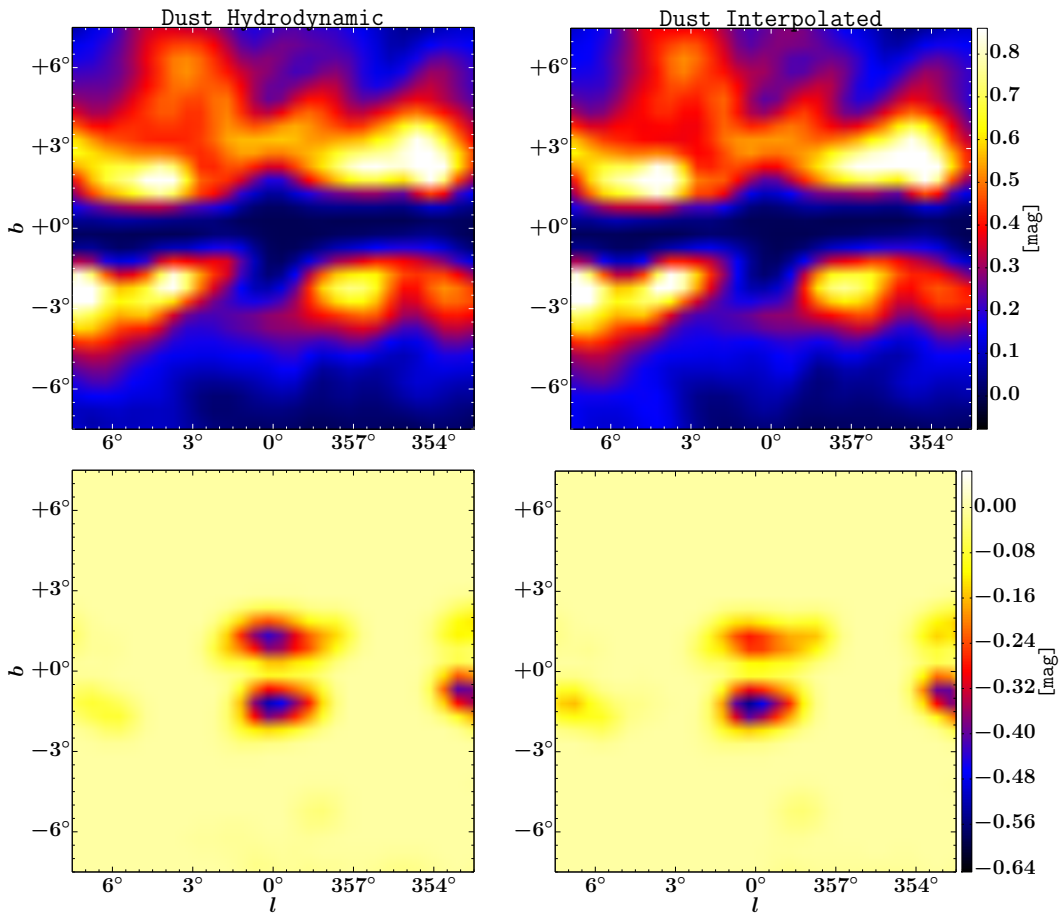

Supplementary Figure 2: Dust reddening E(B-V) positive (top) and negative (bottom) residual maps. The left (right) hand side maps were based on fitting the hydrodynamic (interpolated) HI and CO maps to the E(B-V) reddening map which had be a magnitude cut of 5 mag and higher. For display purposes, Gaussian smoothing with a radius of 0.5° was performed.

Supplementary Table 4: Likelihood analysis results with a Galactic plane mask

Base	Source	$\log(\mathcal{L}_{\rm Base})$	$\log(\mathcal{L}_{\rm Base+Source})$	$\mathrm{TS}_{\rm Source}$	σ	Number of source parameters
baseline	NFW	-430289.1	-430155.5	134	9.8	19
baseline	X-bulge	-430289.1	-430089.2	200	12.5	19
baseline	NP	-430289.1	-429657.8	631	12.9	22×19
baseline+NP	NFW	-429657.8	-429559.9	98	8.0	19
baseline+NP	X-bulge	-429657.8	-429496.6	322	16.5	19
baseline+NP+X-bulge	NFW	-429496.6	-429487.2	19	2	19

See the caption of Table 1 for definitions. After masking the Galactic plane ($|b| < 1^\circ$), the number of new point sources (NP) added to the fit were 22 (see also Supplementary Fig. 11).

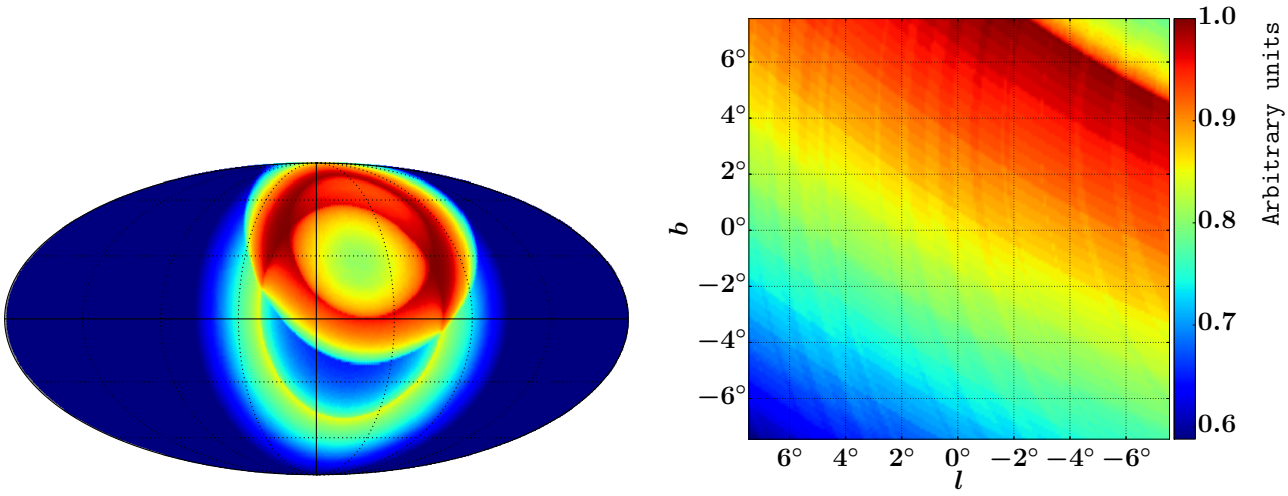

Supplementary Figure 3: Loop I template adapted from ref. 38. A histogram equalized colour mapping is used for display. The map is appropriately normalized, in our region of interest, for analysis with the *Fermi* Science Tools. On the left we show a full sky version of the map in the Mollweide projection and on the right we have zoomed in to our region of interest.

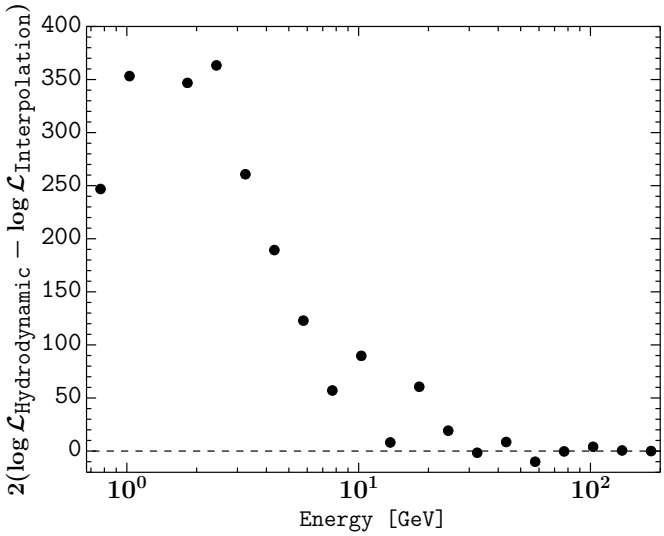

Supplementary Figure 4: Comparison of the log-likelihood obtained for two different interstellar gas models. The likelihood is compared for hydrodynamic[12] gas maps vs the interpolation ones used in the standard Galactic diffuse emission model. Summing over the energy bins gives $\mathrm{TS}_{\mathrm{Hydrodynamic}} = 2 \times 1362$.

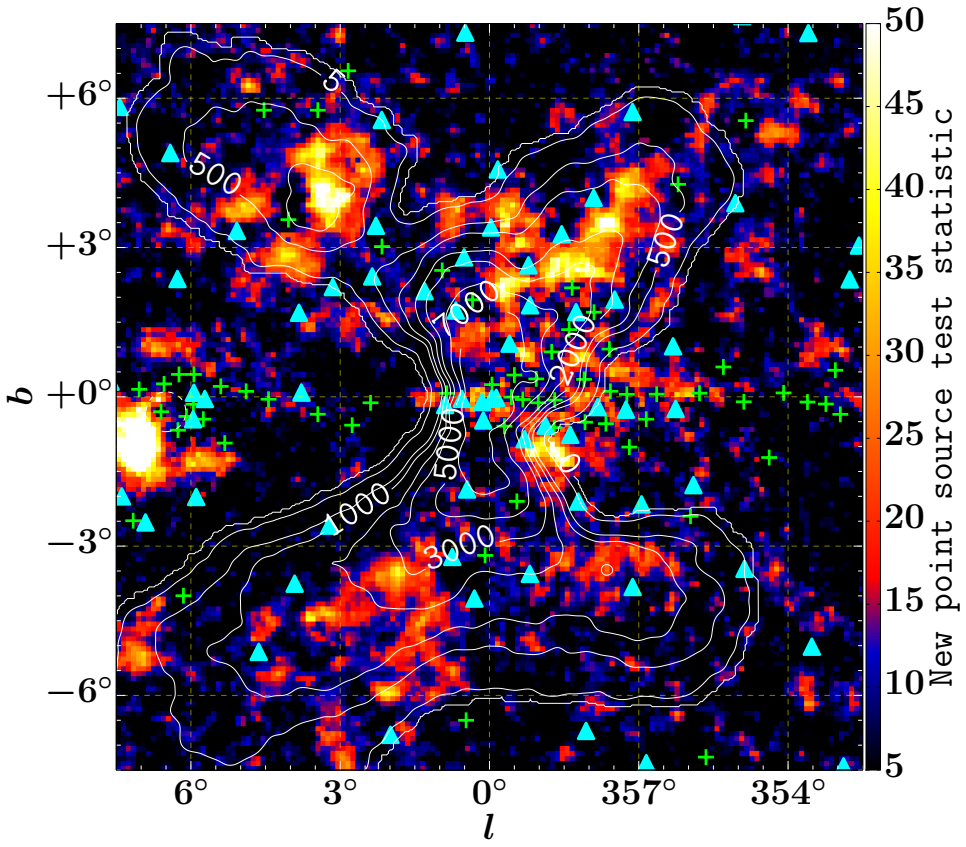

Supplementary Figure 5: Significance map of the $15^\circ \times 15^\circ$ region about the GC output from the `gttsmap` tool after the new point sources have been identified. The energy range shown is 667 MeV−158 GeV. The 3FGL point sources (cyan triangles) and the new point sources (green crosses) are displayed. Supplementary Table 1 summarizes the basic properties of the new point sources.

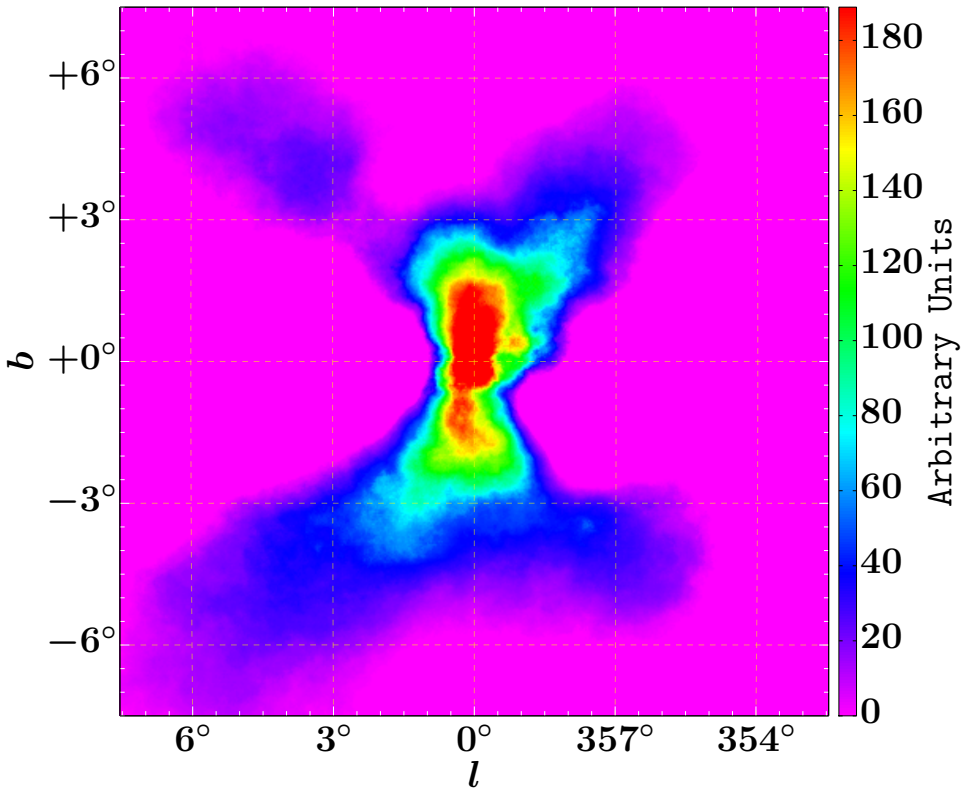

Supplementary Figure 6: The X-bulge template based on the smoothed W1 and W2 WISE data[14] with a best fit exponential bulge component subtracted.

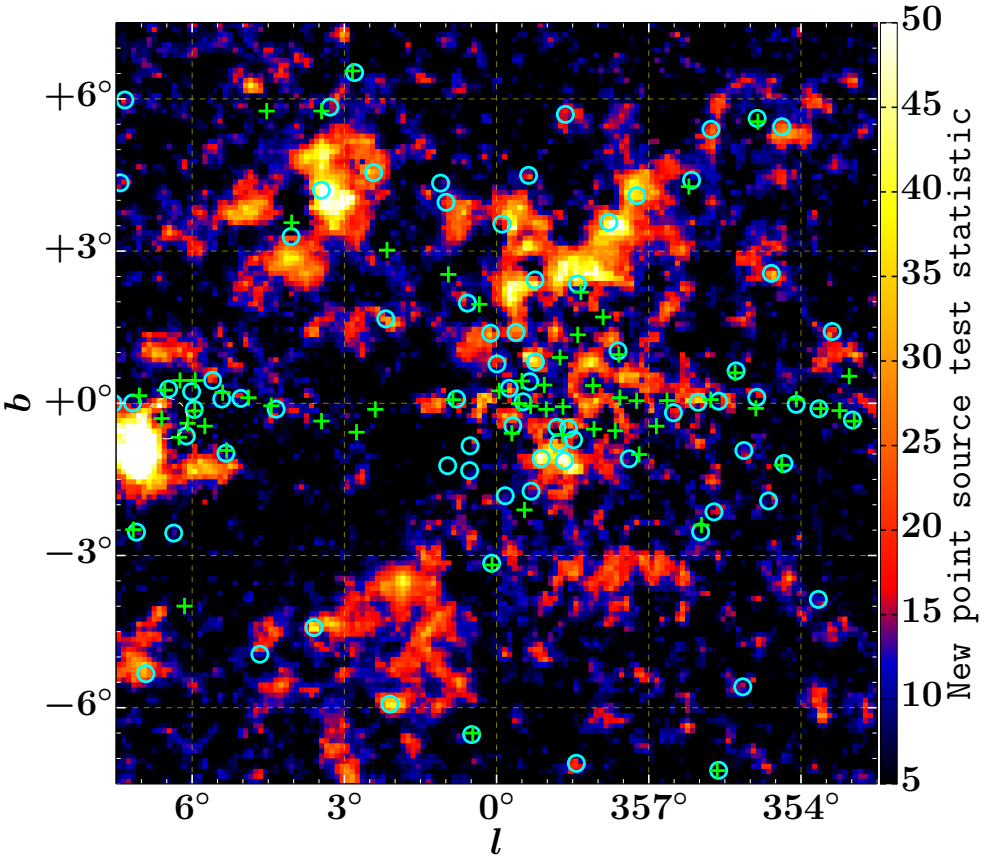

Supplementary Figure 7: Comparison of new gamma-ray point sources in this work vs new point sources in the 2FIG catalog[48]. See caption of Supplementary Fig. 5 for a description of this residual TS map. Cyan circles display the 81 new gamma-ray point sources (not already present in the 3FGL[13]) found in the 2FIG catalog[48]. Green crosses correspond to the 64 new point sources found in this work. Despite the different data sets and background models used in both studies, our analysis confirms the existence of 31 of the new point sources found in 2FIG (see Supplementary Table 1). Note that many undetected 2FIG point source candidates are placed in hot spots in this residual map. It is very likely that by augmenting the time and the photon energy range utilized in this analysis to the same levels used in the 2FIG analysis, such hot spots would be found with greater TS-values and would therefore constitute positive point source detections.

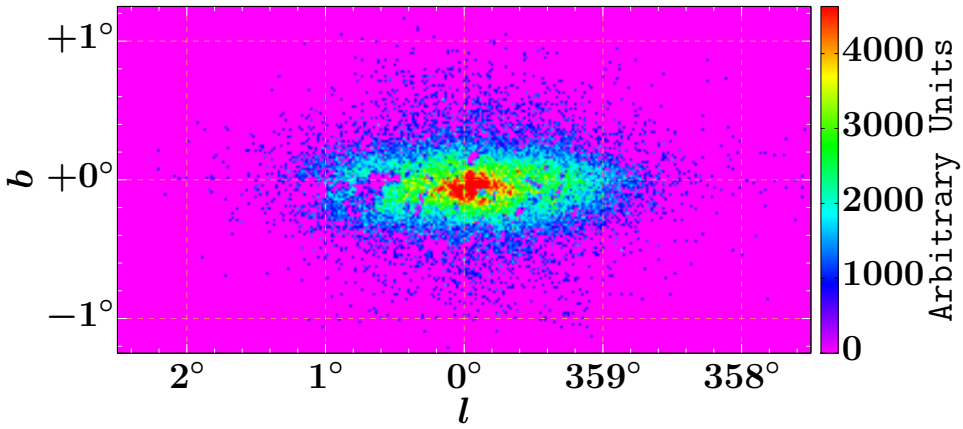

Supplementary Figure 8: The nuclear bulge template based on data from ref. 15 with a best fit exponential disk component subtracted.

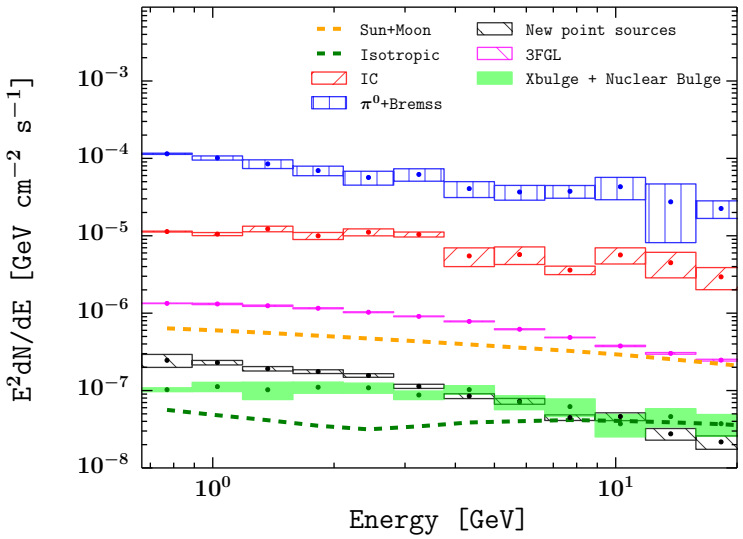

Supplementary Figure 9: Model components. Top: Differential flux of the different components in the $15^\circ \times 15^\circ$ region about the Galactic Center. The model considered in the fit is the *baseline+NP+nuclear bulge+X-bulge* model. To reduce clutter the spectrum of the combined H_I, CO, and dust maps maps are shown as π^0+Bremss. The Loop I spectrum had a low signal to noise for the majority of the bins and so has not been included in the above plot. The box heights represent the the 68% C.I. regions.

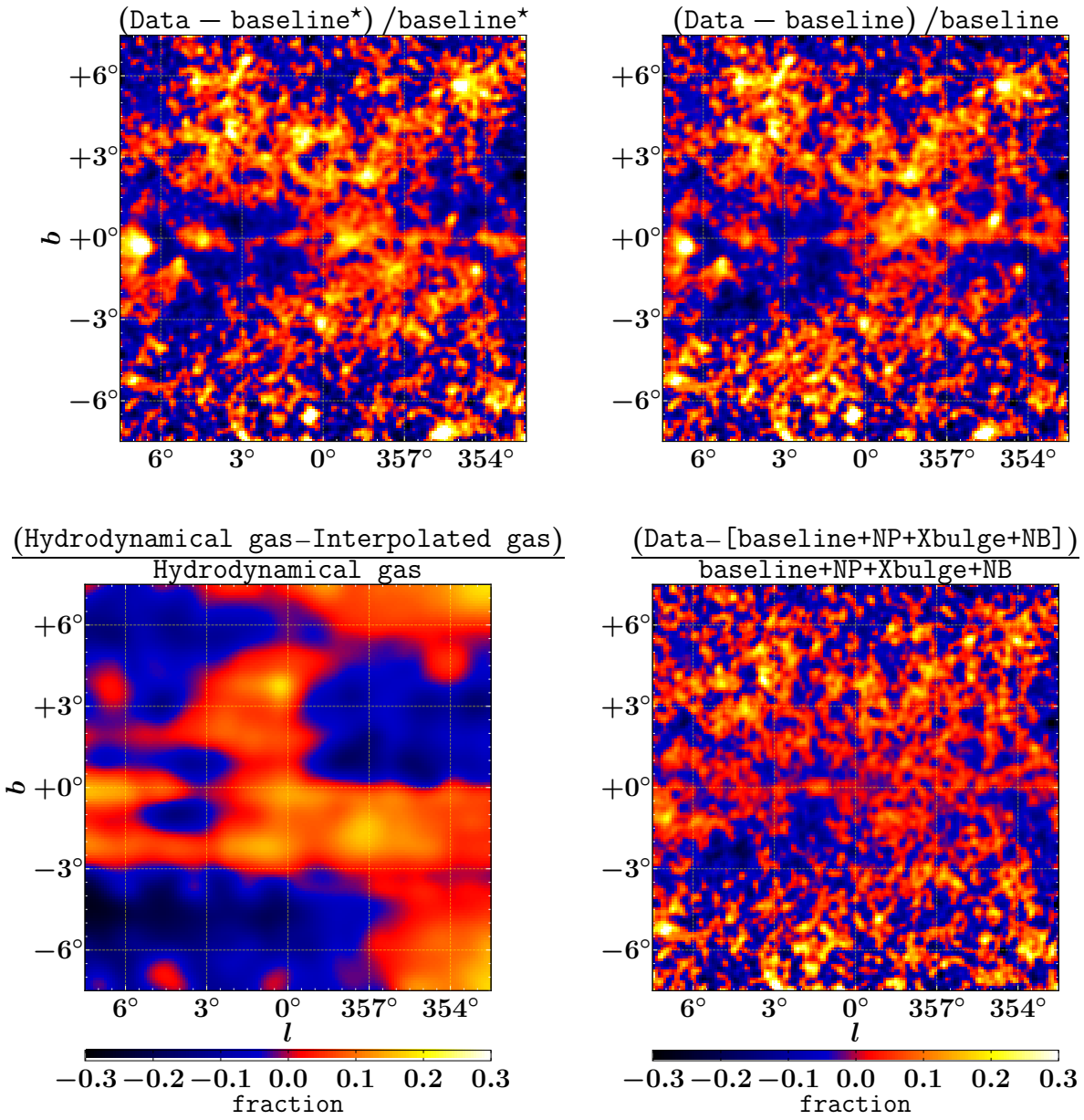

Supplementary Figure 10: Fractional residuals for $E \geq 667$ MeV: Top left: The *baseline** model consists of all 3FGL point sources in the ROI, Loop I, an IC template predicted by GALPROP, the interpolation based gas maps, the recommended isotropic emission map, and a model for the Sun and the Moon. Top right: The *baseline* model is same as the top left, except that it uses the hydrodynamical based gas maps. Bottom left: fractional improvement difference the interpolation based and the hydrodynamical gas maps. Bottom right: Our full model (*baseline*+*NP*+*Xbulge*+*NB*) consisting of the baseline plus the 64 new point sources (NP), an infrared X-bulge template tracing old stars in the Galactic bulge, and a Nuclear Bulge (NB) template. For display purposes, we smoothed these images with a 0.1° Gaussian filter.

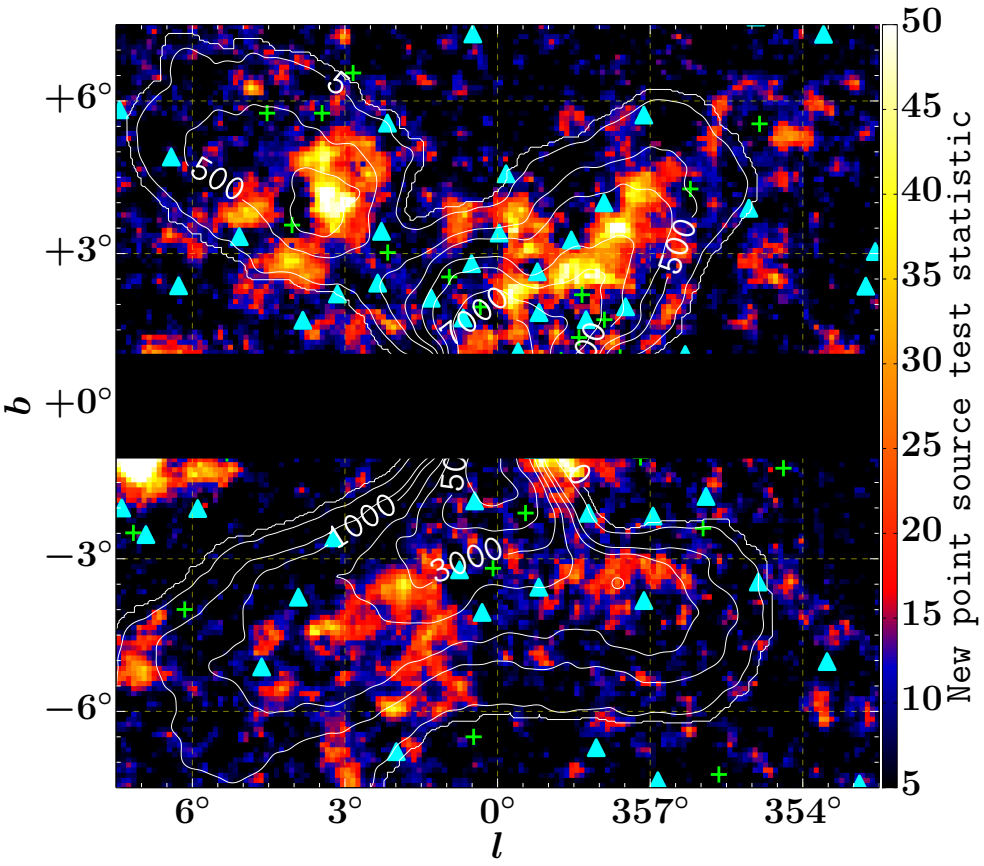

Supplementary Figure 11: Masking of the Galactic plane ($|b| < 1°$)**.** This image displays the ROI for one of our systematic error analyses. The unmasked region contains 22 new point sources. More details of this pipeline are given in the Methods Section and Supplementary Table 4